FLOMEKO 2003
11th IMEKO TC9 Conference on Flow Measurement
Groningen, NETHERLANDS, 12 - 14 May 2003

A CURRENT-TYPE ELECTROMAGNETIC FLOWMETER FOR TWO-PHASE FLOW

Yeh-Chan Ahn[a], Byung Do Oh[b] and Moo Hwan Kim[c]

Department of Mechanical Engineering
Pohang University of Science and Technology
San 31, Hyoja Dong, Pohang, 790-784, Korea
Tel: +82-54-279-2165, +82-54-279-2840, Fax: +82-54-279-3199
E-mail: ayc@postech.ac.kr, bdoh@postech.ac.kr, mhkim@postech.ac.kr (order : a,b,c)

ABSTRACT

The theory for the current-sensing electromagnetic flowmeter was newly developed. The current-sensing flowmeter has a high temporal resolution so that it can be applied to measure the flows with fast transients like two-phase flow. The signal prediction and the calibration of the current-sensing flowmeter in two-phase flow and the measuring of the characteristics of two-phase flow are the major concerns.

To do this, using a finite difference method, the three-dimensional virtual potential distributions for the electrodes of finite size were calculated for single-phase flow, annular flow and slug flow. With the gradient of the virtual potential, the rectilinear weight functions for the single-phase flow and the annular flow which were the main parameter for the conventional voltage-sensing flowmeter were deduced and compared with existing analytic solutions for the point-electrode. There was a reasonable correspondence between the present and existing results. Particularly the axial weight function and the radial weight function for single-phase flow, annular flow and slug flow were newly defined and computed by taking the gradient of the virtual potential.

The flow pattern coefficient f was introduced to simplify the calibration process for two-phase flow. It was calculated from the solved virtual potential distributions of single-phase and two-phase flow. For annular flow, the coefficient was well-fitted with two decaying exponential functions of the normalized film thickness d^*, f=1+1.3 exp(–7d^*)+7.3 exp(–31d^*). For the slug flow, it was provided as a function of the normalized film thickness d^* and the normalized position of a slug bubble tail L^*. The coefficient by the numerical simulation was compared with experimental results obtained by Frequency Response Analyzer (FRA) and Potentiostat/Galvanostat. The comparison clearly showed the agreement between the numerical and the experimental results.

1. INTRODUCTION

Electromagnetic flowmeters have been successfully and accurately used to measure the single-phase liquid mean velocity in various industries for about 40 years. There have been continuous efforts on measuring the characteristics of two-phase flows using an electromagnetic flowmeter, since it makes no pressure drop, can provide fast response to the change of flow. There are many potential applications of electromagnetic flowmeter in two-phase flow.

Electromagnetic flowmeters can be divided into the voltage-sensing and the current-sensing types in the sense of objective signal of measurement. Most of the commercial flowmeters are the voltage-sensing ones because it does not depend on the impedance between electrodes.

One of the difficulties in the design of an electromagnetic flowmeter is that the magnitude of objective signal is too small compared with those of various noises. The main sources of the noises in electromagnetic flowmeters excited by AC power are as follows: (i) transformer electromotive force (emf) by alternating magnetic field (see for example **Hemp** 1991); (ii) power leakage by capacitive and resistive coupling between power and signal circuits (see for example **Tsiknakis** 1988). The noise by the transformer emf can be removed by the phase sensitive detection method with lock-in amplifier. The method shows good performance for both voltage- and current-sensing flowmeters.

The voltage-sensing type uses the low frequency excitation method to remove the noise by power leakage since the noise becomes serious at high frequency excitation, and varies with time, and cannot be quantified precisely. There are many applications, which require a high temporal resolution and a high frequency excitation is needed for flow measurements. Most of two-phase flows vary rapidly and the voltage-sensing flowmeters are failed to measure

the velocity field. In the present study, therefore, the current-sensing flowmeter which is robust to noise by power leakage is introduced. A high temporal resolution can be achieved with the current-sensing flowmeters.

The theory for the voltage-sensing flowmeter was first developed by **Shercliff** (1954). The weight function that represents the degree of the contribution of fluid velocity to the signal in the cross-section of a conduit was proposed and computed for a two-dimensional single-phase flow. **Bevir** (1970) developed the weight vector $\mathbf{W}=\mathbf{B}\times\mathbf{j}$ that is an extension of the weight function to three-dimension using the concept of virtual current **j**. Using the virtual current method, **O'Sullivan and Wyatt** (1983) provided the rectilinear weight functions for electrodes of various numbers, sizes and shapes for the rectilinear flows.

Wyatt (1986) analytically calculated the rectilinear weight function as a series solution for an annular flow as well as a single-phase flow using the two-dimensional flowmeter equation. **Zhang** (1997) investigated the effect of phase distribution on the rectilinear weight function in two-dimensional annular domain with or without eccentricity. The rectilinear weight function with or without eccentricity was provided as series solutions. The estimated errors of the series solutions with finite order increased as the film thickness of annular flow decreased. Since the normalized film thickness of annular flow in practical situations is less than 0.1, a higher order series solution is required to have an accurate solution. **Zhang** (1998) studied the effect of a bubble on the virtual current of an electromagnetic flowmeter numerically with the bubble at various positions along the pipe axis. Two-dimensional assumption was used and the virtual potential was expressed in series. The effect of the bubble sizes was also considered. The change of the virtual current caused by the existence of the bubble was evaluated using deviation and asymmetry. However, the calculation error increased up to 24% as the bubble size normalized with the distance between electrodes increased up to 0.9. In the study of **Lim and Chung** (1998), as well as using the weight function method, the flowmeter equation was solved numerically by the finite volume method with the given velocity field. This study was aimed at comparing the calculation accuracies of two methods. The accuracy of both methods strongly depended on the grid system.

To predict the output for a given velocity profile and to acquire the velocity information from the output, previous researches on voltage-sensing flowmeters were focused on the weight vector $\mathbf{W}=\mathbf{B}\times\mathbf{j}$ (3D), the rectilinear weight function (2D) and the axisymmetric weight function (1D).

As will be discussed in detail in the next section, the calculation of the three-dimensional virtual potential distribution G instead of the weight vector (or function) is very useful for the current-sensing flowmeter. By taking the gradient of the virtual potential, the weight vector (or function), which is the main parameter for the voltage-sensing case, can be easily obtained. Also, the impedance between electrodes required to obtain the flow-induced emf from the output current is equal to the difference of the virtual potentials ΔG at two electrodes if contact impedances between liquid and electrodes can be neglected.

Furthermore, knowledge of the virtual potential distribution enables us to investigate the effect of the arbitrary velocity field on the output current, which means that the theory of electromagetic flowmeters is not restricted to the rectilinear, axisymmetric and fully developed flow field. For example, an electromagnetic flowmeter can measure the liquid velocity experiencing considerable acceleration and deceleration in two-phase slug flow.

In addition, the three-dimensional virtual potential distribution is also important to give the *flow pattern coefficient* f for the current-sensing flowmeter which will be introduced in the next section. The flow pattern coefficient f is proposed to simplify the calibration process for two-phase flows and is defined by the ratio of liquid resistance between electrodes for the two-phase flow with respect to that for the single-phase flow.

2. THEORY OF A CURRENT-SENSING ELECTROMAGNETIC FLOWMETER

For the voltage-sensing flowmeters (see **Figure 2.1.1a**), the unpredictable stray currents (i_1 and i_2) by power leakage flow through the double layers between electrodes and liquid to the ground in liquid because of the signal conditioner with a very high input impedance. Therefore, they produce unpredictable voltages at terminal A and F by the contact impedance of the layer and the resistance of liquid. Since the impedances along two paths for stray current i_1 and i_2 are not symmetric with each other, two voltages at terminal A and F cannot be nulled by the common-mode rejection and the remaining part becomes the noise by power leakage. (Note that the resistances of liquid between point C and ground and between point D and ground vary with respect to the two-phase flow configurations in a conduit.) The noise voltage is much larger than the flow-induced emf. The stray currents problem becomes more serious as the excitation frequency increases since capacitive coupling between signal and power circuit becomes stronger and a higher voltage is needed across the coil if the same magnet current (or magnet field strength) is to be provided. However the high frequency excitation is needed to get a high temporal resolution of the flowmeters.

On the other hand, the current-sensing flowmeters (see **Figure 2.1.1b**) have a signal conditioner with a very low input impedance (**Yu et al.** 1997) for measuring current by the flow-induced emf. The unpredictable stray currents (i_1 and i_2) by power leakage do not flow to the double layers but to the signal conditioner. They become noise currents mixed with signal current i_3 by the flow-induced emf. They are not dependent on the contact impedance or the liquid resistance according to the flow configurations, but on capacitive and resistive coupling between signal and power circuits. It leaves more room for cancelling two opposite currents i_1 and i_2 than voltage-sensing case. If appropriate shieldings around electromagnet windings and signal wires are provided, noise currents can be cancelled out for the most part in spite of high frequency excitation.

Another point to be discussed for the current-sensing case is the relevance of the signal current i_3 to the contact impedance and the liquid resistance in a conduit. To predict the signal current i_3 from the flow-induced emf, the impedances along the paths of signal current i_3 should be evaluated. The liquid resistance is related with the liquid conductivity (sensitive to temperature) and the flow configurations of two-phase flows. As the liquid conductivity and (or) the flow configuration in a two-phase flow vary with time, the signal current i_3 changes also. The signal current i_3 is affected by the contact impedances of the double layers (or by the impedance between the liquid and the electrodes). The contact impedance is very sensitive to the material of electrodes and the electrochemical properties of liquid, and there are intensive discussions on the problem under the subject of electrochemistry (**Glasstone** 1942; **Macdonald** 1987).

In short, the current-sensing flowmeters with the phase sensitive detection method is immune to both noises said previously, and guarantee the ability to measure the signal current i_3 by the flow-induced emf though it is complex to predict the liquid velocity from the signal current i_3 because the impedances along the paths of signal current i_3 should be evaluated.

For conventional voltage-sensing flowmeters, the potential distribution U by the fluid motion inside a flow tube is described by the Poisson equation (**Shercliff** 1962; **Bevir** 1970)

$$\nabla^2 U = \mathrm{div}(\mathbf{v}\times\mathbf{B}). \tag{2.1}$$

To evaluate the potential difference ΔU between two electrodes by the motion, a virtual problem (see **Figure 2.1.2**) was introduced, which is to obtain the distribution of virtual current density $\mathbf{j}$ in the stationary flow with the unit current through the electrodes at the boundary. Thus, $\mathbf{j}$ depends on the electrode shape, on electrical conditions on the flowmeter wall, and on the flow configurations (for two-phase flow case).

Let U and $\mathbf{j}^m$ be the potential and current induced by the motion and G and $\mathbf{j}$ those set up when unit current is passed between the electrodes with no motion. Then Ohm's law gives

$$j_i^m = \sigma_{ij}[-\partial U/\partial x_j + (\mathbf{v}\times\mathbf{B})_j], \tag{2.2}$$

$$j_i = -\sigma_{ij}\partial G/\partial x_j . \tag{2.3}$$

Let S_A and S_B be surfaces around the electrode A and B and t the volume of the moving fluid. Then because $\nabla\cdot\mathbf{j}^m = \nabla\cdot\mathbf{j} = 0$ and $\mathbf{j}^m$ and $\mathbf{j}$ =$O(1/R^3)$ for large R, Gauss's theorem gives, when there is no contact impedance between each electrode and fluid,

$$\int_{S_A+S_B}(U\mathbf{j} - G\mathbf{j}^{\mathbf{m}})\cdot d\mathbf{S} = \int(\nabla U\cdot\mathbf{j} - \nabla G\cdot\mathbf{j}^{\mathbf{m}})dt . \tag{2.4}$$

If no current is drawn from the electrodes during operation as a flowmeter then

$$\int_{S_B}\mathbf{j}^{\mathbf{m}}\cdot d\mathbf{S} = -\int_{S_A}\mathbf{j}^{\mathbf{m}}\cdot d\mathbf{S} = 0, \tag{2.5}$$

$$\int_{S_B}\mathbf{j}\cdot d\mathbf{S} = -\int_{S_A}\mathbf{j}\cdot d\mathbf{S} = 1. \tag{2.6}$$

Also, U and G are constants on the electrodes (which are taken to have infinite conductivity). Substituting Equation (2.2), (2.3) and (2.5) into Equation (2.4), we find

$$(U_B - U_A)\int_{S_B}\mathbf{j}\cdot d\mathbf{S} = \iiint_t\left[-\sigma_{ij}\frac{\partial U}{\partial x_i}\frac{\partial G}{\partial x_j} + \sigma_{ij}\frac{\partial G}{\partial x_i}\frac{\partial U}{\partial x_j} - \frac{\partial G}{\partial x_i}\sigma_{ij}(\mathbf{v}\times\mathbf{B})_j\right]dt , \tag{2.7}$$

and using the symmetry of σ_{ij} and using Equation (2.3), Equation (2.7) can be represented by

$$\Delta U\int_{S_B}\mathbf{j}\cdot d\mathbf{S} = \iiint_t \mathbf{v}\cdot\mathbf{W}\,dt , \tag{2.8a}$$

or using Equation (2.6)

$$\Delta U \cdot (1\mathrm{A}) = \iiint_t \mathbf{v} \cdot \mathbf{W}\, dt \ . \tag{2.8b}$$

Here, **v** is the velocity vector, t is the volume of the moving fluid, ΔU is $U_B - U_A$ and **W= B×j** is the weight vector, which is the cross-product of the magnetic flux **B** and the virtual current density **j**. **Bevir**(1970) presented Equation (2.8b) in other form by omitting the unit current,

$$\Delta U = \iiint_t \mathbf{v} \cdot \mathbf{W}\, dt \ , \tag{2.9}$$

which seems to lose the unit consistency.

When the flow is rectilinear and axisymmetric and the transverse magnetic field is uniform with the point electrodes, the potential difference ΔU between electrodes can be derived as

$$\Delta U_{SP} = \frac{\left[\iiint_t \mathbf{v} \cdot \mathbf{W}\, dt\right]_{SP}}{\int_{S_B} \mathbf{j} \cdot d\mathbf{S}} = 2Bv_{mSP}R \ , \tag{2.10a}$$

or

$$\Delta U_{SP} = \frac{\left[\iiint_t \mathbf{v} \cdot \mathbf{W}\, dt\right]_{SP}}{(1\mathrm{A})} = 2Bv_{mSP}R \ , \tag{2.10b}$$

for a single-phase liquid flow (**Shercliff** 1962),

$$\Delta U_{TP} = \frac{\left[\iiint_t \mathbf{v} \cdot \mathbf{W}\, dt\right]_{TP}}{\int_{S_B} \mathbf{j} \cdot d\mathbf{S}} = 2Bv_{mTP}R \ , \tag{2.11a}$$

or

$$\Delta U_{TP} = \frac{\left[\iiint_t \mathbf{v} \cdot \mathbf{W}\, dt\right]_{TP}}{(1\mathrm{A})} = 2Bv_{mTP}R \ , \tag{2.11b}$$

for annular flow and bubbly flow which can be considered as a homogeneous gas-liquid mixture without slip (**Wyatt** 1986). Here, the subscripts *SP* and *TP* denote single- and two-phase flow respectively and v_m is liquid mean velocity. Equation (2.10) and (2.11) can approximately be used for the small practicable finite-size electrodes.

For the slug flow with axisymmetric velocity field and geometry, the volume integral in Equation (2.8b) reduces to

$$\Delta U_{TP} = \iiint_t \mathbf{v} \cdot \mathbf{W}\, dt \ /(1A) = 2p \iint \left[v_r(r,z)W_r(r,z) + v_z(r,z)W_z(r,z)\right] r dr dz \ /(1A) \equiv 2B\tilde{v}_{mTP}R \ . \tag{2.12}$$

Here, $\tilde{v}_{mTP}$ is a estimated liquid mean velocity. $W_r(r,z)$ is the radial weight function and $W_z(r,z)$ is the axial weight function. The weight functions are defined by

$$W_r(r,z) = \frac{1}{2p}\int_0^{2p} W_r(r,q,z)dq = -\frac{B}{2p}\int_0^{2p} \sin q \, \frac{\partial G}{\partial z}\, dq \ , \tag{2.13}$$

and

$$W_z(r,z) = \frac{1}{2p}\int_0^{2p} W_z(r,q,z)dq = \frac{B}{2p}\int_0^{2p} \frac{\partial G}{\partial y}\, dq \ , \tag{2.14}$$

for the uniform transverse magnetic field *B*.

For the current-sensing flowmeter, the same virtual problem (see **Figure 2.1.2**) introduced for the voltage-sensing flowmeter is also useful. When there is no contact impedance between each electrode and fluid, Equation (2.4) is also available. If the current *i* by the motion is drawn from the electrodes during operation as a flowmeter then

$$\int_{S_B} \mathbf{j}^{\mathbf{m}} \cdot d\mathbf{S} = -\int_{S_A} \mathbf{j}^{\mathbf{m}} \cdot d\mathbf{S} \equiv i \ , \tag{2.15}$$

$$\int_{S_B} \mathbf{j} \cdot d\mathbf{S} = -\int_{S_A} \mathbf{j} \cdot d\mathbf{S} = 1 . \tag{2.16}$$

For the current-sensing flowmeter, two electrodes are shorted and grounded for measuring the current by the motion. Therefore

$$U_A = U_B = 0 . \tag{2.17}$$

Substituting Equation (2.2), (2.3) and (2.17) into Equation (2.4), we find

$$\int_{S_B} (G_A - G_B)\mathbf{j}^m \cdot d\mathbf{S} = \iiint_t \left[-s_{ij} \frac{\partial U}{\partial x_i}\frac{\partial G}{\partial x_j} + s_{ij}\frac{\partial G}{\partial x_i}\frac{\partial U}{\partial x_j} - \frac{\partial G}{\partial x_i} s_{ij} (\mathbf{v}\times\mathbf{B})_j \right] dt , \tag{2.18}$$

if there is no contact impedance in the double layers. Using the symmetry of s_{ij} and Equation (2.3), Equation (2.18) can be represented by

$$\int_{S_B} \Delta G \mathbf{j}^m \cdot d\mathbf{S} = \iiint_t \mathbf{v} \cdot \mathbf{W} \, dt , \tag{2.19}$$

where $\Delta G = G_A - G_B$. In comparison with voltage-sensing case (see Equation 2.8), both have the same volume integral, $\iiint_t \mathbf{v} \cdot \mathbf{W} dt$ and $\mathbf{W}$ is related with the gradient of virtual potential G. The calculation of the virtual potential G is very useful to both types of flowmeter (see section 3). Knowledge of the virtual potential G enables us to investigate the effect of arbitrary velocity fields on flowmeter outputs. The theory of electromagnetic flowmeters has been mainly applied to the rectilinear, axisymmetric and fully developed flow field. Two-phase flow is, however, not like this in general. For example, the liquid velocity field along a slug unit experiences considerable acceleration and deceleration in slug flow (**Mi et al.** 2001).

When the flow is rectilinear and axisymmetric and the transverse magnetic field is uniform with the point electrodes, Equation (2.19) with Equation (2.10) and (2.11) gives

$$\left[\int_{S_B} \Delta G \mathbf{j}^m \cdot d\mathbf{S}\right]_{SP} = 2Bv_{mSP}R\int_{S_B} \mathbf{j} \cdot d\mathbf{S} , \tag{2.20a}$$

or

$$\left[\int_{S_B} \Delta G \mathbf{j}^m \cdot d\mathbf{S}\right]_{SP} = 2Bv_{mSP}R \cdot (1\mathrm{A}) , \tag{2.20b}$$

for a single-phase liquid flow,

$$\left[\int_{S_B} \Delta G \mathbf{j}^m \cdot d\mathbf{S}\right]_{TP} = 2Bv_{mTP}R\int_{S_B} \mathbf{j} \cdot d\mathbf{S} , \tag{2.21a}$$

or

$$\left[\int_{S_B} \Delta G \mathbf{j}^m \cdot d\mathbf{S}\right]_{TP} = 2Bv_{mTP}R \cdot (1\mathrm{A}) , \tag{2.21b}$$

for annular flow and bubbly flow which can be considered as a homogeneous gas-liquid mixture without slip. Here, the subscripts *SP* and *TP* denote single- and two-phase flow respectively.

With Equation (2.15) and for the small practicable finite-size electrodes with an infinite conductivity, the current i by the fluid motion can approximately be presented by

$$i_{SP} = \frac{2Bv_{mSP}R\int_{S_B} \mathbf{j} \cdot d\mathbf{S}}{\Delta G_{SP}} , \tag{2.22a}$$

or

$$i_{SP} = \frac{2Bv_{mSP}R \cdot (1\mathrm{A})}{\Delta G_{SP}} , \tag{2.22b}$$

for a single-phase liquid flow,

$$i_{TP} = \frac{2Bv_{mTP}R\int_{S_B} \mathbf{j} \cdot d\mathbf{S}}{\Delta G_{TP}} , \tag{2.23a}$$

or

$$i_{TP} = \frac{2Bv_{mTP}R \cdot (1\mathrm{A})}{\Delta G_{TP}} , \tag{2.23b}$$

for annular flow and bubbly flow. Then i_{TP} can be rewritten as

$$i_{TP} = \frac{2Bv_{mTP}R\cdot(1\mathrm{A})}{\Delta G_{TP}} = \frac{i_{SP}}{v_{mSP}}\frac{\Delta G_{SP}}{\Delta G_{TP}}v_{mTP} \equiv \frac{i_{SP}}{v_{mSP}}\frac{1}{f}v_{mTP}\,, \tag{2.24}$$

for annular flow or homogeneous bubbly flow using Equation (2.22b) and (2.23b),

and $$i_{TP} = \frac{i_{SP}}{2v_{mSP}R\cdot(1\mathrm{A})}\frac{1}{f}\iint\left[-v_r(r,z)\int_0^{2p}\sin q\,\frac{\partial G}{\partial z}dq + v_z(r,z)\int_0^{2p}\frac{\partial G}{\partial y}dq\right]rdrdz \equiv \frac{i_{SP}}{v_{mSP}}\frac{1}{f}\tilde{v}_{mTP}\,, \tag{2.25}$$

for slug flow using Equation (2.12), (2.13), (2.14), (2.19) and (2.22b). Here, f is the flow pattern coefficient related with the flow configuration only. Void fraction (for bubbly flow) or film thickness (for annular flow) is all about flow configuration and the relative position of nose to electrode plane and bubble length are enough for slug flow with Taylor bubbles. $\tilde{v}_{mTP}$ is a estimated liquid mean velocity.

The calculation of the three-dimensional virtual potential distribution G is also important to give the flow pattern coefficient f for the current-sensing flowmeter. The flow pattern coefficient f is proposed to simplify the calibration process for two-phase flow and is defined by the ratio of liquid resistances between electrodes for two-phase flow with respect to that for single-phase flow. The output of the current-sensing flowmeter depends on the liquid resistance between electrodes when neglecting the contact impedance in the double layer. The liquid resistance is related with the liquid conductivity (sensitive to temperature) and the flow configuration. Introducing the flow pattern coefficient f and using the calibration data of single-phase flow can separate the dependency on the output of the flow configuration from that of the liquid conductivity.

In practical application to two-phase annular flow, one should have the single-phase flow calibration chart and the flow pattern coefficient f as a function of flow configuration with Equation (2.24) or (2.25). The single-phase flow calibration chart by the manufacturer will give $\frac{i_{SP}}{v_{mSP}}$ in the right-hand sides which includes the fluid conductivity effect depending on the fluid species and the fluid temperature variation. Flow configurations in bubbly, annular and slug flow can be easily measured using at most two impedance meters (void fraction or film thickness, void propagation speed and bubble length can be obtained.) and if the functional form of f with respect to flow configuration was made numerically or experimentally in advance, the measured flow configurations give the value of f. Therefore the current output i_{TP} gives the liquid mean velocity v_{mTP} for bubbly and annular flow (or the estimated liquid velocity $\tilde{v}_{mTP}$ for slug flow).

3. Numerical Analysis

3.1 Single-Phase and Annular Flow

3.1.1 Governing equation and the boundary conditions for virtual potential

To solve the virtual problem introduced before, the governing equation for the virtual current or the virtual potential G can be written in the cylindrical coordinates for the computational domain in **Figure 3.1.1**,

$$\nabla^2 G = \frac{1}{r}\frac{\partial}{\partial r}r\frac{\partial}{\partial r}G + \frac{1}{r^2}\frac{\partial^2}{\partial q^2}G + \frac{\partial^2}{\partial z^2}G = 0\,. \tag{3.1.1}$$

Let us define G as $\mathbf{j} = \nabla G$ from now on for convenience.

The boundary conditions in the axial (z) direction are the homogeneous Neumann condition since the infinite domain is assumed and no current can pass through the end planes. The length of the pipe L_z in the computational domain is determined not to disturb the result due to insufficient extents in the axial direction. When L_z/R is larger than 4, it is sufficient to carry out the computation without the end effect.

For the azimuthal (q) direction, skew symmetric condition (see **Figure 3.1.1**) is applied since the two electrodes are located on the mutually symmetric location. Therefore, the computational domain is composed of the only upper half cylinder, and at the center plane (with respect to the electrodes), the homogeneous Dirichlet condition is imposed.

In the radial (r) direction, a step-like distribution is used on the electrode and the homogeneous Neumann condition is used at other place. The shape of the electrode located on the center in the axial direction of the pipe is a

square and the size L_e/R is 1/6.35 for the comparison with experimental setup in **Figure 3.1.10**. The boundary conditions can be expressed as follows:

$$\frac{\partial}{\partial z}G = 0 \qquad \text{at } z = 0 \text{ and } z = L_z, \tag{3.1.2}$$

$$G = 0 \qquad \text{at } q = 0 \text{ and } q = p, \tag{3.1.3}$$

$$\frac{\partial}{\partial r}G = E(q, z) \qquad \text{at } r = R, \text{ on the electrode}, \tag{3.1.4}$$

$$\frac{\partial}{\partial r}G = 0 \qquad \text{at } r = R, \text{ otherwise}, \tag{3.1.5}$$

$$\frac{\partial}{\partial r}G = 0 \qquad \text{at } r = R_i, \tag{3.1.6}$$

where R_i is the radius of the gas core. For the single-phase flow, R_i=0, a singular point treatment is required. Physically the centerline is not a special line but there need special treatment due to the factor 1/r in the radial operator. The singularity at the centerline is avoided by placing the first grid point half-spacing away from the centerline (see section 3.1.2).

3.1.2 Numerical method

A finite difference method is used to solve the governing equation. The central difference scheme is used for the spatial discretization. To avoid the massive matrix inversion, the problem is reconstructed as pseudo-unsteady one:

$$\frac{\partial}{\partial t}G = \frac{1}{r}d_r\left(r d_r G\right) + \frac{1}{r^2}d_q^2 G + d_z^2 G, \tag{3.1.7}$$

where d_r, d_q and d_z denote the difference operator in r-, q- and z-direction respectively. To discretize the artificial temporal term, the implicit Crank-Nicolson scheme is used and then, Equation (3.1.7) is factorized to read,

$$\left[\mathbf{I} - \frac{\Delta t}{2r}d_r\left(r d_r\right)\right]\left[\mathbf{I} - \frac{\Delta t}{2r^2}d_q^2\right]\left[\mathbf{I} - \frac{\Delta t}{2}d_z^2\right]G^{(n+1)} = \left[\mathbf{I} + \frac{\Delta t}{2}d^2\right]G^{(n)}, \tag{3.1.8}$$

where $d^2 = \frac{1}{r}d_r\left(r d_r\right) + \frac{1}{r^2}d_q^2 + d_z^2$ and superscript n denotes the virtual time step. Thus, when the difference $G^{(n+1)}$-$G^{(n)}$ is less than the given criterion (in the present computation, it is set to 10^{-10}) $G^{(n)}$ is considered to reach its steady solution. The use of factorization is to decouple the operator, and the matrix reduces to tridiagonal matrices.

To implement the Neumann boundary condition without further approximation, the first and the last grid points of the radial and axial directions are located on the half-spacing away from the boundaries like the pressure grid point in the marker-and-cell (MAC) staggered grid system. For example, the discretized equation in the axial direction adjacent to the end plane $k=N_z$ is

$$[\cdots]\left[G^{(n+1)}\Big|_{i,j,Nz} - \frac{\Delta t}{\left(h^z_{Nz} + h^z_{Nz-1}\right)}\left(d_z G^{(n+1)}\Big|_{i,j,Nz+1/2} - d_z G^{(n+1)}\Big|_{i,j,Nz-1/2}\right)\right] = G^{(n)}\Big|_{i,j,Nz} + \cdots, \tag{3.1.9}$$

where i, j and k are running indices for the radial, azimuthal and axial direction respectively and h^z_k is the grid spacing in z-direction. Since the first term in the parentheses, $d_z G^{(n+1)}\Big|_{i,j,Nz+1/2}$ is determined by the boundary condition, which is imposed as the Neumann condition, there is no further approximation in implementation of the boundary conditions.

The solutions depend only on the electrode shape when the overall geometry and the magnitude of the current on the electrodes are determined. In the previous two-dimensional simulations (**Zhang** 1997), the point electrode is assumed so that the delta function is used as the boundary condition. If the virtual current is computed with the present finite difference method, the point electrode cannot be achieved. Therefore, we choose the electrode of finite size and simulate a say, *area-electrode type*, whose area is same as that in the experimental setup. Since the physical extents of the electrode are about 0.05 and 0.04 of the circumferential and the axial dimension (L_z/R=4) of the computation domain, respectively (see **Figure 3.1.2**), there need intensive grid points to resolve the stiff potential field near the electrode. To alleviate the problem, two stretching functions are used. For radial direction, a tangent hyperbolic func-

tion (**Thompson et al.** 1985) is used, which is modified to have a dense grid near the wall (or the electrode),

$$\frac{r(x)}{R} = \frac{1}{a_r}\tanh\left(\frac{x}{2}\ln\frac{1+a_r}{1-a_r}\right)\left(\frac{R-R_i}{R}\right)+\frac{R_i}{R}, \tag{3.1.10}$$

where a_r is the stretching parameter for the radial direction. When a_r goes to 1, the grid is clustered toward the wall. For the axial and azimuthal direction, the other stretching function is used,

$$\frac{z(V)}{L_z} = \frac{1}{2}\left(1-\ln\frac{1+a_z(1-2V)}{1-a_z(1-2V)}\Big/\ln\frac{1+a_z}{1-a_z}\right), \tag{3.1.11}$$

$$q(h) = \frac{p}{2}\left(1-\ln\frac{1+a_q(1-2h)}{1-a_q(1-2h)}\Big/\ln\frac{1+a_q}{1-a_q}\right), \tag{3.1.12}$$

where a_z is the stretching parameter for the axial direction and similarly a_q is for the azimuthal direction. When a_z and a_q go to 1, the grid becomes denser around the electrode placed on the center of the computational domain. **Figure 3.1.3** and **Figure 3.1.4** show the stretching functions with typical stretching parameters.

The grid size effect is tested by increasing the number of grid points twice for each direction (up to 100×200×200 points for N_r, N_q and N_z), and the difference of the potential field is less than 1%. Therefore the simulations are carried out with 50×100×100 points. The effect of the stretching parameters is also investigated with 50×100×100 grid points, when a_r, a_q and a_z are larger than 0.9, the differences of the solution between each other are less than 0.5%. Most simulations are carried out with a_r=0.95, a_q=0.9 and a_z=0.9.

Since the finite nature of the numerical method, the current on the electrode could not have the step increment. If such a finite increment is imposed as the boundary condition, the grid size dependency of the solution becomes dominating, as the increment is larger. To resolve the problem, the smoothing of the boundary current is applied. The most ideal smoothing can be made by using an unitary function, whose Fourier transform have the value only at the zero wavenumber (**Lighthill** 1980). Unitary functions, however, consist of the improper integral and cannot be easily implemented. Therefore, a polynomial curve fit, which makes smooth the profile of the current up to the first order derivatives, is made and can be represented

$$E(z)L_e = \begin{cases} 0 & \text{for } \bar{z} \le -\frac{L_e}{2}-b \\ -\frac{1}{4b^3}\left(\bar{z}+\frac{L_e}{2}\right)^3+\frac{3}{4b}\left(\bar{z}+\frac{L_e}{2}\right)+\frac{1}{2} & \text{for } -\frac{L_e}{2}-b \le \bar{z} \le -\frac{L_e}{2}+b \\ 1 & \text{for } -\frac{L_e}{2}+b \le \bar{z} \le \frac{L_e}{2}-b \\ \frac{1}{4b^3}\left(\bar{z}-\frac{L_e}{2}\right)^3-\frac{3}{4b}\left(\bar{z}-\frac{L_e}{2}\right)+\frac{1}{2} & \text{for } \frac{L_e}{2}-b \le \bar{z} \le \frac{L_e}{2}+b \\ 0 & \text{for } \bar{z} \ge \frac{L_e}{2}+b \end{cases}, \tag{3.1.13}$$

where, b is the *diffusion parameter* which determines the fitting length and $\bar{z} = z - L_z/2$. Likewise, *E(q)* can be constructed. As the boundary condition *E(q,z)* (see Equation 3.1.4), the product of the *E(q)* and *E(z)* is used. The effect of the diffusion parameter is tested for b=0.04 (about 25 % of the length of the electrode), b=0.08 and b=0, and the potential value at the center of the electrode have less than 0.5% differences between each other. In the present study, b=0.04 is used (see **Figure 3.1.2**).

As already mentioned, a virtual unsteady scheme combined with the factorization is used to avoid the massive matrix inversion. The Crank-Nicolson scheme is always a stable scheme such that it has no limits regarding time steps since any oscillation is damped after a few time steps. However, by the stiffness, the solution depends highly on the initial condition. If the zero potential distribution is given with a larger timestep then a wrong but converged solution is resulted. Thus, the non-dimensional (virtual) time step $\Delta t^* = \dfrac{\Delta t}{\min(\Delta r^2, \Delta(rq)^2, \Delta z^2)}$ is lower than 0.3 in the computations to avoid the stiffness problem. To reduce the computing time due to the small time increment, the intermediate computations are carried out with a larger time step and then, the computation of the proper time step is made by using the intermediate one as an initial condition.

The numerical accuracy can be totally estimated from the mean-value theorem, which can be written as

$$\left| \int_0^{L_z} \int_0^{p} \int_{R_i}^{R} \frac{\partial G}{\partial y} r dr dq dz - R \right|. \tag{3.1.14}$$

However, since the gradients $\partial G/\partial y$ are approximated by the second order finite difference scheme, the integrals in Equation (3.1.14) overestimate the numerical errors of the computations. Instead of Equation (3.1.14), the error is estimated by the integration of the virtual current on the symmetric plane using the continuity of the virtual current (see **Figure 3.1.1**):

$$\left| R \int_0^{L_z} \int_0^{p} E(q, z) dq dz - \left(\int_{R_i}^{R} \int_0^{L_z} \left. \frac{\partial G}{\partial y} \right|_{q=0} dz dr + \int_{R_i}^{R} \int_0^{L_z} \left. \frac{\partial G}{\partial y} \right|_{q=p} dz dr \right) \right|. \tag{3.1.15}$$

There are some variations in the error because the grid resolution is changed with the size of gas core but the errors are about 10^{-5} for all of the computations, which correspond to the finite difference errors.

3.1.3 Numerical Results and Comparison with experiments

Figure 3.1.5 shows the rectilinear weight function normalized by the axisymmetric weight function. **Figure 3.1.5(a)** is the numerical result for electrodes of finite size and for single-phase flow, which is compared with the *Shercliff's weight function* shown in **Figure 3.1.5(b)** for point electrodes and for single-phase flow. The Shercliff's weight function can be written as

$$W(r/R, q) = \frac{2B}{pR} \frac{1 + (r/R)^2 \cos 2q}{1 + 2(r/R)^2 \cos 2q + (r/R)^4}. \tag{3.1.16}$$

Figure 3.1.5(c) is the numerical result for electrodes of finite size and for R_i/R = 0.5. **Figure 3.1.5(d)** shows the analytical series solution which is calculated up to 200th term for point electrodes and for R_i/R = 0.5. It was derived by **Wyatt** (1986) as a series form:

$$W(r/R, q) = \frac{2B}{pR} \left\{ \sum_{m=0}^{\infty} (-1)^m (r/R)^{2m} \cos 2mq + \sum_{m=0}^{\infty} (-1)^m A_m \left[(r/R)^{2m} \cos 2mq + (r/R)^{-2(m+1)} \cos 2(m+1)q \right] \right\}, \tag{3.1.17}$$

where $A_m = e^{2m+1}/(1- e^{2m+1})$ and $e = R_i^2/R^2$. The values of the rectilinear weight function of the numerical results are the same as those of the analytical results except for in the neighborhood of electrodes. **Figure 3.1.5(e)** and **Figure 3.1.5(f)** are the contour plots of the weight function from the numerical results for R_i/R = 0.8 and for R_i/R = 0.95 respectively.

The Shercliff's weight function has a saddle point at the origin where the value of the normalized weight function is one. For non-zero void fractions, four saddle points are located at each quadrant and there are two points with zero-weighting-value at $q = \pm p/2$ on the gas-liquid interface, which are current stagnation points and local maxima are located at $q = 0$ and p on the gas-liquid interface. The saddle points approach to the electrodes as the void fraction increases. Since the local maximum value is increased due to the contraction of the current passage at $q = 0$ and p as the void fraction increases, the influential zone around the local maximum is extended, and the zone around global maxima at electrodes is contracted relatively. That means when the weight function is computed by using the series solution, higher order correction should be considered to have an accurate solution as the film thickness of the annular flow become thinner.

The use of the rectilinear weight function is limited to the flow with the rectilinear velocity profile $\mathbf{v} = (0,0,v_z(r,q))$. However, for measuring the liquid mean velocity for more complicate profiles, the weight vector **W** or the virtual potential distribution is required. From **Figure 3.1.6** to **Figure 3.1.8**, the virtual potential distributions normalized with electrode potential are represented for the single-phase flow and annular flows with different film thicknesses. Contours around the electrodes are squeezed in the radial direction by the non-conducting gas core so that a considerable virtual current flows further downstream and upstream along z direction.

Figure 3.1.9 shows the flow pattern coeffficients with respect to the normalized film thickness $d^*=(R-R_i)/R$ obtained by the numerical method and compared with the experimental results. The flow pattern coefficient is well-fitted with two decaying exponential functions, $f=1+1.3 \exp(-7d^*)+7.3 \exp(-31d^*)$. For $d^* > 0.2$, the first two terms in the fitting function sufficiently shows the behavior of the coefficient. When d^* is greather than 0.5, the flow pattern

coefficient is nearly 1 since the virtual potential difference between the electrodes decreases steeply and becomes nearly constant after d^*=0.5.

It should be noted that the effect of the contact impedance is neglected in the numerical simulations. However, the contact impedance is very important because the current passing through the double layers is the stray current noise for the voltage-sensing flowmeter and the objective signal for the current-sensing flowmeter. To measure and investigate the contact impedance, the impedance between electrodes and the liquid resistance are measured with the impedance spectroscopy using Solartron 1255 HF Frequency Response Analyzer (FRA) and EG&G Potentiostat/Galvanostat Model 273A. **Figure 3.1.10** shows the schmetics of the experimental setup. Two platinum electrodes (2 mm OD) are installed (recessed 0.3 mm from the internal surface of the flow tube) in the polycarbonate tube (1 inch ID) with precisely machined acrylic rods to simulate the gas cores of various sizes. Eight micrometers are installed at the top and the bottom of the tube for precise positioning of the rod. Then the impedance for the platinum electrode and tap water system is measured with the 5mV sinusoidal wave without a DC bias.

Figure 3.1.11 shows the Nyquist plot of the impedance for the single phase flow (d^*= 1) and the annular flow (d^*= 0.04) measured with the FRA and the Potentiostat/Galvanostat. The room temperature is controlled within 23.4^{o}C ± 0.4^{o}C during experiments since the impedance is sensitive to the temperature. When the excitation frequence is higher than 100 Hz, only resistive component remains and the imaginary part of impedance goes to zero. It can be seen apparently in Bode plot (**Figure 3.1.13**) since the phase angle approaches to zero as frequency increases. From the Nyquist plot, an equivalent resistance and capacitance circuit can be constructed. **Figure 3.1.12** shows the modeled circuit. R_1 is the resistor for tap water and R_2 is the resistor, C_2 and C_3 are the capacitors for electrochemical phenomena around the double layer. The value of R_1 is 37.366 kΩ for single-phase flow (d^*= 1) and 123.45 kΩ for the annular flow with d^* = 0.04 at 23.4^{o}C. The flow pattern parameter f is measured and plotted with the numerical results in the **Figure 3.1.9**. There are small differences between the numerical results and the experimental data and are mainly caused by the electrodes recessed by 0.3 mm. To investigate the effect of the room temperature on f, the temperature varied about 10 ^{o}C but there is no effect on the parameter. The flow pattern parameter f can be viewed as the ratio of *cell constants* in electrochemistry (**Glasstone** 1942) and the ratio of cell constants is belived to be independent of temperature (or the liquid conductivity) and to depend on the film thickness.

It is interesting to note for the design of an electromagnet that the condition of $L_z/R > 4$ is sufficient to carry out the computation without the end effect as shown in the section 3.1.1. Therefore, the end effect of the imposed magnetic field in z direction is negligible if the field can be approximated to be uniform from $z = 0$ to $z = 4R$. In addition, the uniform length of magnetic field which is necessary for making the flowmeter outputs immune to the end effect increases as the normalized film thickness d^* decreases.

3.2 Slug Flow

One of the most complicated flow patterns is slug flow since the liquid axial velocity along a slug unit experiences considerable acceleration or deceleration. Slug flow can be decomposed into annular flow and bubbly flow geometrically so that the same relation as that for bubbly or annular flow may be applied (**Mi** 1998). However the decomposition and the adopting the same relation results in errors since the velocity field of slug flow violates the fully development and the rectilinear assumption and an electromagnetic flowmeter may see the completely different flow geometry from bubbly or annular flow when the nose or the tail of Taylor bubble passes the electrode plane. This might be one of the origins of max. 15% error in liquid flowrate (**Mi** 1998).

In the previous sections, the calculation of the three dimensional virtual potential distributions in annular domains gave the output prediction for both voltage- and current-sensing flowmeters by providing of the weight function and the functional form of the flow pattern coefficient f. The same procedure can be applied to slug flow and then the error by the decomposition can be estimated.

In order to assess the flowmeter output in slug flow, a simplified model is proposed, where the shape of Taylor bubble is approximated by a finite cylinder with the same as the axial length of the bubble. In this study, the slug bubbles longer than the axial length of the computation domain L_z are considered in order that the shape approximation is meaningful. Recall that the length of the pipe L_z in the computational domain was determined not to disturb the result due to insufficient extents in the axial direction and when L_z/R was larger than 4, it was sufficient to carry out the computation without the end effect for R_i/R = 0 to 0.95 (see section 3.1.1).

For the modeled slug flow, the flow pattern coefficient f is provided as a function of the normalized film thickness

and the normalized position of the bubble tail. The radial weight function and the axial weight function are defined and calculated to estimate the possible errors in liquid mean velocity. The virtual current distribution is compared with the two-dimensional analysis of **Zhang**(1998) using point electrodes.

3.2.1 Numerical Computation

The same governing equation as in annular flow is used for the computational domain in **Figure 3.2.1**. The boundary conditions are also same except at the gas-liquid interface. Instead of Equation (3.1.6), the following condition is imposed.

$$\frac{\partial}{\partial n}G = 0 \qquad \text{at the interface.} \tag{3.2.1}$$

The singular point treatment at the pipe axis across liquid region is also required as in annular flow.

The region inside the bubble is treated as a dead block. As **Figure 3.2.2** shows for the z-directional sweep, the diagonal and off-diagonal components corresponding to the dead block are assigned to 1 and 0 respectively and the right-hand side is set to 0. The Neumann boundary condition at the node adjacent to the dead block is imposed by giving a remedy in the next row of the tri-diagonal matrix and the right-hand side. Because of the dead block treatment, grid points are located in bubble, and hence, the radial stretching function is, instead of Equation (3.1.10), represented as,

$$\frac{r(x)}{R} = \frac{1}{a_r}\tanh\left(\frac{x}{2}\ln\frac{1+a_r}{1-a_r}\right), \tag{3.2.2}$$

where a_r is the stretching parameter for the radial direction.

The error is estimated by the integration of the virtual current on the symmetric plane using the continuity of the virtual current:

$$\left| R\int_0^{L_z}\int_0^{p} E(q,z)\,dq\,dz - \left(\iint \left.\frac{\partial G}{\partial y}\right|_{q=0} dz\,dr + \iint \left.\frac{\partial G}{\partial y}\right|_{q=p} dz\,dr \right) \right|. \tag{3.2.3}$$

There are some variations in the error but the errors are about 10^{-4} for all of the computations, which correspond to the finite difference errors.

3.2.2 Numerical Results

Figure 3.2.3 to **Figure 3.2.6** show the *axial weight functions* divided by the magnetic flux density *B*, which is defined in Equation (2.14). The axial weight functions vary with the film thickness $d^*=d/R$ and the bubble position which is represented by its tail position $L^*=L/R$. Contour level 0.1 for all figures means that the azimuthal average of the y-component of the virtual current density is 0.248% of the virtual current density imposed at electrode. Therefore it can ensure that the end effect of the imposed magnetic field in *z* direction is negligible if the field can be approximated to be uniform from $z^*=z/R=0$ to 4.

For annular flows (labeled by *a* in the figures) and a single-phase flow (labeled by *h*), the axial weight function is symmetric with respect to $z^*=z/R=2$ (electrode). The figures labeled by (b) to (g) depict the in-between cases, say slug flows, with the asymmetry of the contours. When these figures are compared with those of the annular flow with the same film thickness and the single-phase flow, the weighting extent in z direction is reduced as the bubble moves up. This results from the detouring of the virtual current toward the path with a relatively lower resistance. The same thing can be remarked if the cases with the same position of the bubble tail but with the different film thickness are compared with each other.

Figure 3.2.7 to **Figure 3.2.10** show the *radial weight functions* divided by the magnetic flux density *B*, which is defined in Equation (2.13). The radial weight functions vary with the film thickness d^* and the bubble position which is represented by its tail position $L^*=L/R$. It also shows that the end effect of the imposed magnetic field in *z* direction is negligible if the field can be approximated to be uniform from $z^*=z/R=0$ to 4.

For annular flows (labeled by *a* in the figures) and a single-phase flow (labeled by *h*), the radial weight function related with the z-component of the virtual current is anti-symmetric with respect to $z^*=z/R=2$ (electrode plane).

In the figures labeled by (g) and (h), there are stagnant lines with zero level which means that the radial velocities

on the lines do not contribute to the output signal. The line moves downward to be horizontal as the bubble rises. For the cases of L^*=2.5 (*g* in the figures) with the different film thickness, the line moves up with decreasing film thickness. The radial weight function is more localized around the electrode than the axial weight function, so that the radial velocity in the region around the pipe center does not make a considerable effect.

Mi(1998) assumed that slug flow can be decomposed into annular flow and bubbly flow geometrically and that the same relation (see last part of Equation (2.12) or (2.25)) as that for bubbly or annular flow may be applied. It is very natural and simple. However the error in the estimated liquid mean velocity is inevitable as mentioned in the starting part of the section 3.2. For the voltage- and current-sensing flowmeters, the estimated liquid mean velocity can be rewritten as

$$\tilde{v}_{m,TP}\Big|_{z=2R} = \int \left[\bar{v}_r(z)q(z) + \bar{v}_z(z)p(z)\right]dz, \tag{3.2.4}$$

where

$$p(z) \equiv \int \frac{pW_z(r,z)}{BR\cdot(1\mathrm{A})}\,rdr, \tag{3.2.5}$$

$$q(z) \equiv \int \frac{pW_r(r,z)}{BR\cdot(1\mathrm{A})}\,rdr, \tag{3.2.6}$$

$$\bar{v}_z(z) \equiv \frac{1}{p(z)}\int v_z(r,z)\frac{pW_z(r,z)}{BR\cdot(1\mathrm{A})}\,rdr, \tag{3.2.7}$$

$$\bar{v}_r(z) \equiv \frac{1}{q(z)}\int v_r(r,z)\frac{pW_r(r,z)}{BR\cdot(1\mathrm{A})}\,rdr, \tag{3.2.8}$$

and $\tilde{v}_{mTP}\Big|_{z=2R}$ means the estimated liquid mean velocity at electrode plane. Particularly, $p(z)$ is called by the *axial weight density function* because its integration with respect to z is unity from the mean-value theorem of harmonic function. Hence the estimation error can be measure as

$$error = \int \left[\bar{v}_r(z)q(z) + \bar{v}_z(z)p(z)\right]dz - v_{m,TP}\Big|_{z=2R}, \tag{3.2.9}$$

where $v_{mTP}\Big|_{z=2R}$ is the real liquid velocity at the electrode plane.

The axial weight density functions $p(z)$ for d^*=0.1 are shown in **Figure 3.2.11** to **Figure 3.2.14**. The dotted line is for the single-phase flow (L^*=4) and the dash-dot line is for the annular flow (L^*=0). The solid line represents the axial weight density function for the in-between case with different L^* for each figure. The sharp decrease in the density function represents the bubble tail. In slug flow, the detouring of the virtual current makes the increase of the density function in the liquid slug and the decrease in the liquid film compared with single-phase flow and annular flow respectively. The relative portions of the over-weighted density function for the liquid slug are 27% (for L^*=1), 46% (for L^*=1.5), 93% (for L^*=2.3) and 96% (for L^*=2.5). Instead of $\bar{v}_z(z)$, the radially averaged liquid velocity data from **DeJesus**(1997) using the photochromic dye activation method which denoted by solid triangles are overlapped to evaluate roughly the error in Equation (3.2.9). The data are acquired for the case of a rising Taylor bubble (length: 11.5cm) in a stagnant liquid. It is obvious that the axial velocity is abruptly reduced in liquid slug due to the wake region following the bubble. The velocity indicated by the arrow in each figure can be considered to be equal to the real liquid mean velocity at the electrode, $v_{mTP}\Big|_{z=2R}$. Considering the velocity profile measured along z direction and the axial weight density function, the estimation errors measured by Equation (3.2.9) (only axial term in the estimated velocity is considered) are about +20% for L^*=1 and +30% for L^*=1.5. However, for L^*=2.3 and L^*=2.5, the errors are almost negligible because of the relatively small portions of the axial weight density function for the liquid film. These effects make the shape of the estimated velocity variation with respect to time (or L^*) blunt around bubble tail. The above error estimation used only axial term in the estimated velocity. If the radial component of the velocity is considered, the estimation will be better. However it is not easy because of the lack of the measured velocity data.

The relative portion of the axial weight density function for the liquid slug and the asymmetry of the function are shown in **Figure 3.2.15**. The asymmetry is defined by the ratio of the difference between integration areas below and

over electrode position (z^*=2) to total integration area of the axial weight density function.

The radially integrated radial weight functions $q(z)$ for d^*=0.1 are shown in **Figure 3.2.16** to **Figure 3.2.19**. The dotted line is for the single-phase flow (L^*=4) and the dash-dot line is for the annular flow (L^*=0). The solid line represents $q(z)$ for the in-between case with different L^* for each figure. The abrupt change in $q(z)$ is occurred at the bubble tail. The relative portion of $q(z)$ for the liquid slug and the asymmetry of $q(z)$ are shown in **Figure 3.2.20**. The asymmetry is defined by the ratio of the difference between the absolute integration areas below and over electrode position (z^*=2) to total absolute integration area.

The current-sensing flowmeter requires that the flow pattern coefficient f should be known in advance. From the computed virtual potential differences between two electrodes, the coefficient shown in **Figure 3.2.21** or **Figure 3.2.22** is obtained. The coefficient f is the function of the nondimensionalized film thickness d^* and the nondimensionalized bubble tail position L^* for the bubble longer than $4R$. The coefficient f is almost unity for the larger L^* than 2.5 and for the larger d^* than 0.5.

Zhang(1998) computed the 2D virtual current field for the point electrode (line electrode in 3D space). The domain is divided into sub-domains. In each of the sub-domains, the potential of the virtual current is expressed in series with unknown coefficients. An alternating method is used to find the unknowns. The calculation error is estimated by,

$$\max\left|\frac{1}{2a}\int_{-b}^{b}\int_{-a}^{a}\frac{\partial G}{\partial y}\,dydz-1\right|. \tag{3.2.10}$$

where a is the half of the distance between electrodes and b is the half axial span of computational domain. The calculation error is 0.24 for the bubble with $a_o/a=b_o/b$=0.9. Here $2a_o$ and $2b_o$ are bubble lengths in the transverse and axial direction of the domain. In the present study the accuracy is within 10^{-4} for all the cases. The distribution of the virtual current for the square bubble with the length 0.5 is shown in **Figure 3.2.23**.

4. CONCLUSIONS

The significance of this study is that the theory for the current-sensing electromagnetic flowmeter was newly developed. The current-sensing flowmeter has a high temporal resolution so that it can be applied to measure the flows with fast transients like two-phase flow. The rectilinear, axisymmetric and fully developed flow field has been considered so far, as long as the electromagnetic flowmeter is concerned. However, the flowmeter output can be now predicted for arbitrary flow field from the present study.

In numerical analysis, the following conclusions were drawn. It was shown that the three-dimensional virtual potential distribution G is very useful to predict the response of the current-sensing flowmeter. Using a finite difference method, the three-dimensional virtual potential distributions for the electrodes of finite size were calculated for annular flow, single-phase flow and slug flow.

Taking the gradient of the virtual potential, the rectilinear weight functions for the annular flow and the single-phase flow, which were the main parameter for the conventional voltage-sensing flowmeter, were deduced and compared with existing analytic solutions for the point-electrode. There was a reasonable correspondence between the present and existing results. Particularly the axial weight function and the radial weight function for annular flow, single-phase flow and slug flow were newly defined and computed by taking the gradient of the virtual potential.

The flow pattern coefficient f was specially devised to simplify the calibration process for two-phase flow. It was calculated from the solved virtual potential distributions of single-phase and two-phase flow. For annular flow, the coefficient was well-fitted with two decaying exponential functions of the normalized film thickness d^*, f=1+1.3 exp(–7d^*)+7.3 exp(–31d^*). For the slug flow, it was provided as a function of the normalized film thickness d^* and the normalized position of a slug bubble tail L^*. The coefficient by the numerical simulation was compared by experiments using Frequency Response Analyzer (FRA) and Potentiostat/Galvanostat. The comparison clearly showed the agreement between the numerical and the experimental results.

The effect of presence of the bubble on the virtual potential distribution can be negligible if d^*>0.5 or L^*>2.5. It was shown that the end effect due to the shortage of magnetic field in flow direction (z direction) could be negligible if the field was approximated to be uniform from z = 0 to z = 4R (R is the pipe inner radius).

The velocity field of slug flow is neither rectilinear nor fully developed. The estimated velocity from the flowmeter indication should have errors. The evaluation method of the errors was developed.

ACKNOWLEDGEMENTS

This work was supported by National Research Laboratory of the Korean Ministry of Science and Technology and Brain Korea 21 by the Korean Ministry of Education. We thank Dr. Jae-Woo Kim during the experiments with the frequency response analyzer for assistance and valuable discussion.

REFERENCES

Bevir, M. K., The theory of induced voltage electromagnetic flowmeters, J. Fluid Mechanics, **43**, part 3, 577-590, 1970.

DeJesus, J.M., An experimental and numerical investigation of two-phase slug flow in a vertical tube, Ph.D. Thesis, U. of Toronto, Canada, 1997.

Glasstone, S., An introduction to electrochemistry, Van Nostrand, New York, 1942.

Hemp, J., Theory of eddy currents in electromagnetic flowmeters, J. Physics D: Applied Physics, **24**, 244-251, 1991.

Lighthill, M.J., Introduction to Fourier analysis and generalised functions, Cambridge University Press, London, 1980.

Lim, K.W. and Chung, M.K., Relative errors in evaluating the electromagnetic flowmeter signal using the weight function method and the finite volume method, Flow Meas. Instrum., **9**, 229-235, 1998.

Macdonald, J.S., Impedance spectroscopy: Emphasizing solid materials and systems, John Wiley & Sons, New York, 1987.

Mi, Y., Two-phase flow characterization based on advanced instrumentation, neural networks, and mathematical modeling, Ph.D. Thesis, Purdue Univ., USA, 1998.

Mi, Y., Ishii, M. and Tsoukalas, L.H., Investigation of vertical slug flow with advanced two-phase flow instrumentation, Nuclear Eng. Des., **204**, 69-85, 2001.

O'Sullivan, V.T. and Wyatt, D.G., Computation of electromagnetic flowmeter characteristics from magnetic field data: III. Rectilinear weight functions, J. Phys. D: Appl. Phys., **16**, 1461-1476, 1983.

Shercliff, J.A., Relation between the velocity profile and the sensitivity of electromagnetic flowmeters, J. Applied Physics, **25**, 817-818, 1954.

Shercliff, J.A., The theory of electromagnetic flow-measurement, Cambridge University Press, 1962.

Thompson, J.F. et al., Numerical grid generation: foundations and applications, North-Holland, New York, 1985.

Tsiknakis E., Novel excitation waveforms and signal processing for electromagnetic flowmeters, Ph.D Thesis, University of Bradford, 1988.

Wyatt, D.G., Electromagnetic flowmeter sensitivity with two-phase flow, Int. J. Multiphase Flow, **12**(6), 1009-1017, 1986.

Yu, P.L., Zhang, C.Y. and Zmood, R.B., Wide-band low-input-impedance trans-impedance amplifiers for instrumentation application, Meas. Sci. Tech. **8**, 1351-1355, 1997.

Zhang, X.Z., The effect of the phase distribution on the weight function of an electromagnetic flow meter in 2D and in the annular domain, Meas. Sci. Technol., **8**, 1285-1288, 1997.

Zhang, X.Z., 2D analysis for the virtual current distribution in an electromagnetic flow meter with a bubble at various axis positions, Meas. Sci. Technol., **9**, 1501-1505, 1998.

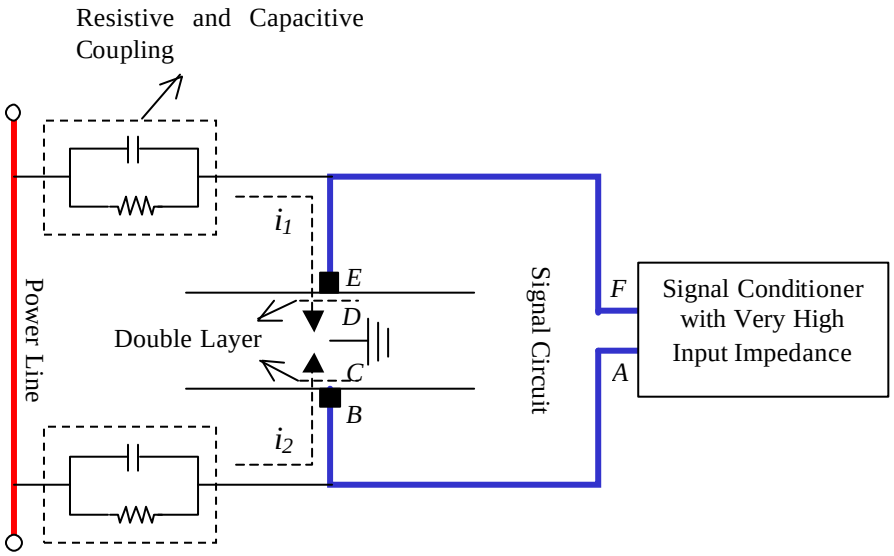

(a) Voltage-sensing flowmeter

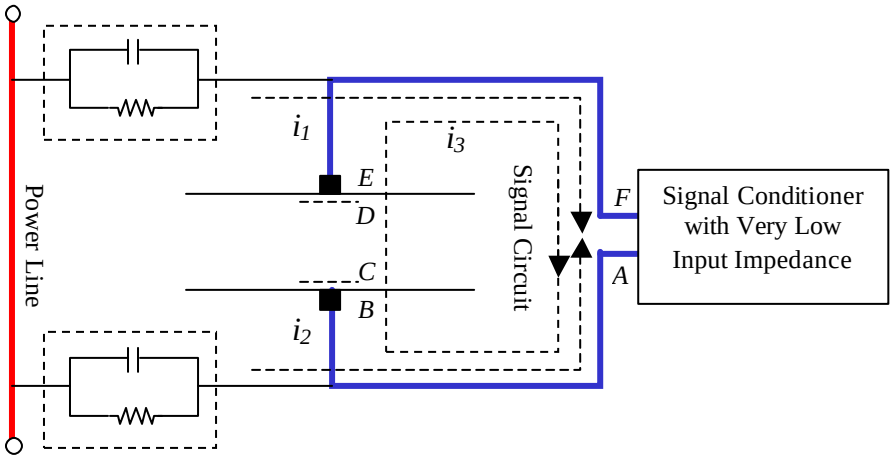

(b) Current-sensing flowmeter

Figure 2.1.1 Voltage-sensing vs. current-sensing flowmeter.

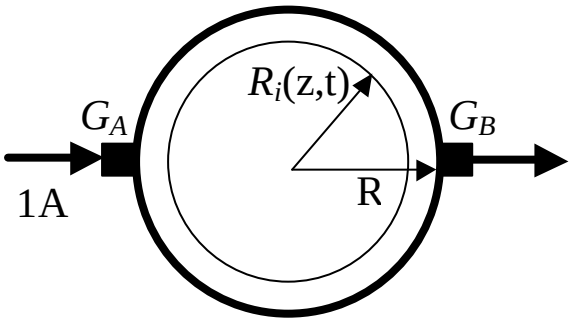

(a) Virtual configuration

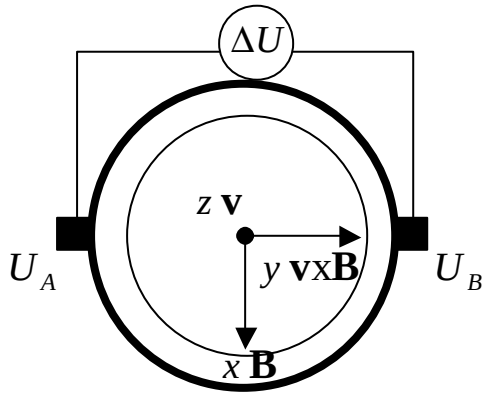

(b) Real configuration (voltage-sensing case)

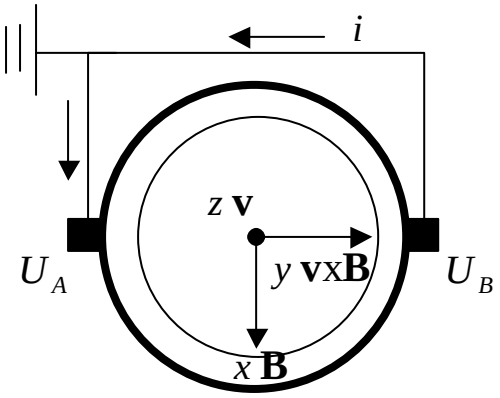

(c) Real configuration (current-sensing case)

Figure 2.1.2 The virtual and real configuration for both flowmeters.

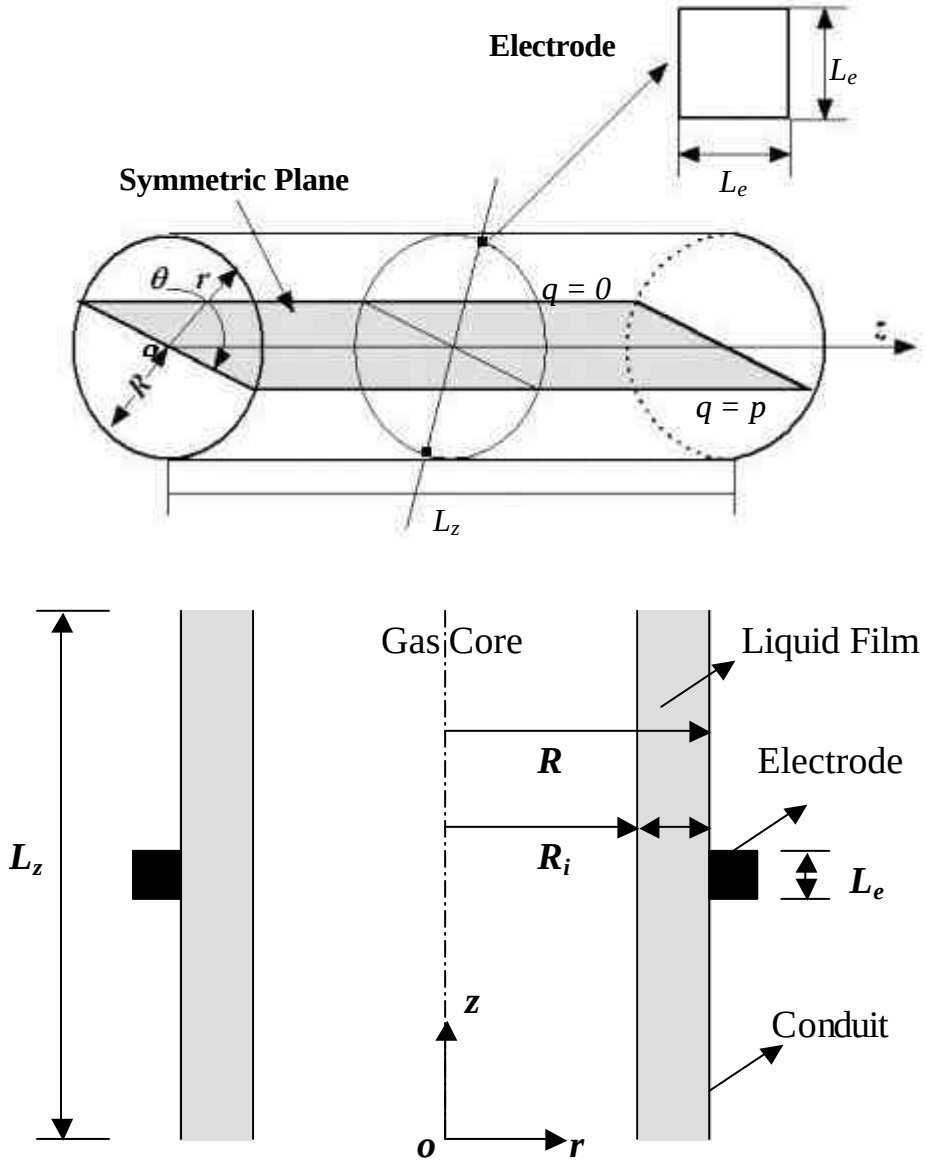

Figure 3.1.1 Schematics for the computational domain.

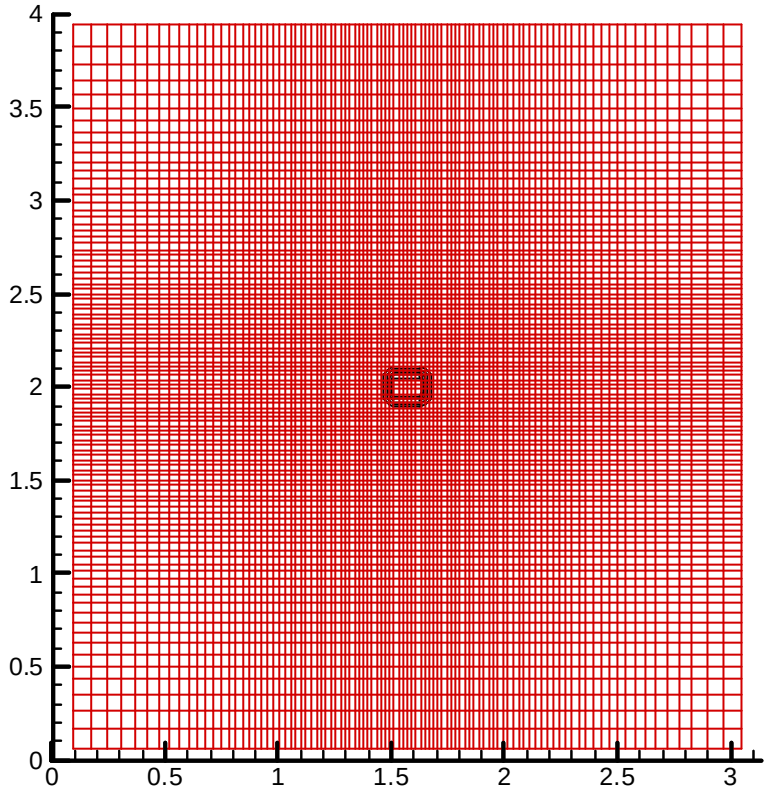

Figure 3.1.2 Plot of the grid system and the electrode shape (presented by the contour whose level denotes magnitude of the current density $E(q,z)$ at the boundary) in the q-z plane (a_z=a_q =0.9 and N_z×N_q=100×100).

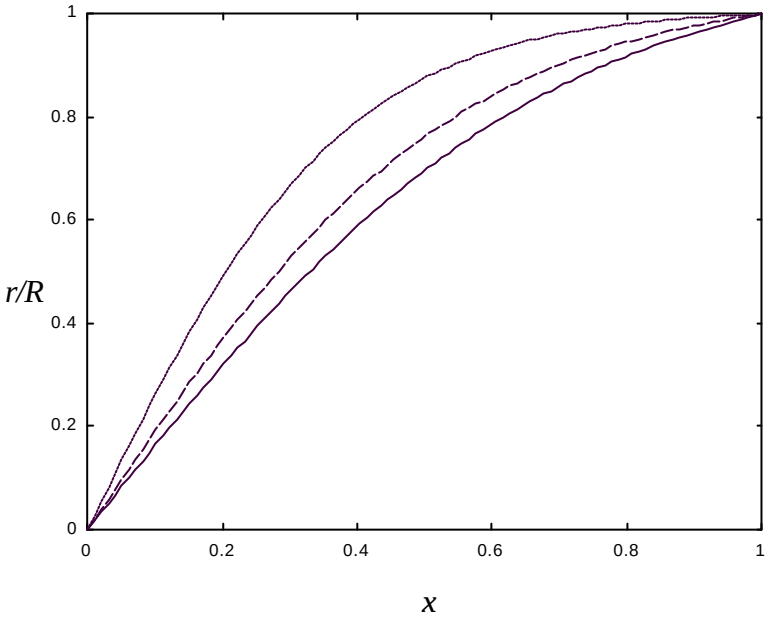

Figure 3.1.3 Stretching function for the radial direction (R_i=0): ———, a_r=0.90; – – –, a_r=0.95; ·····, a_r=0.99.

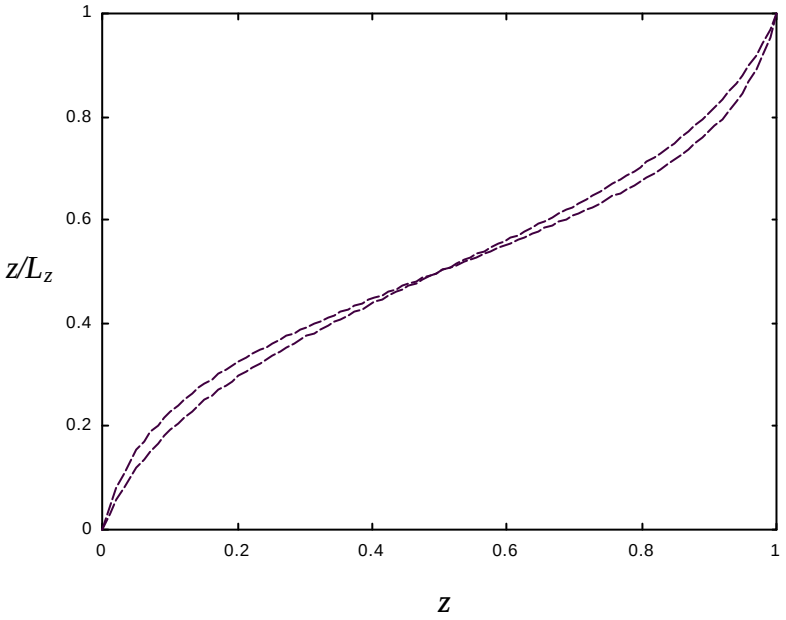

Figure 3.1.4 Stretching function for the axial and the circumferential direction (here, only axial direction): ———, a_z=0.95; – – –, a_z=0.90.

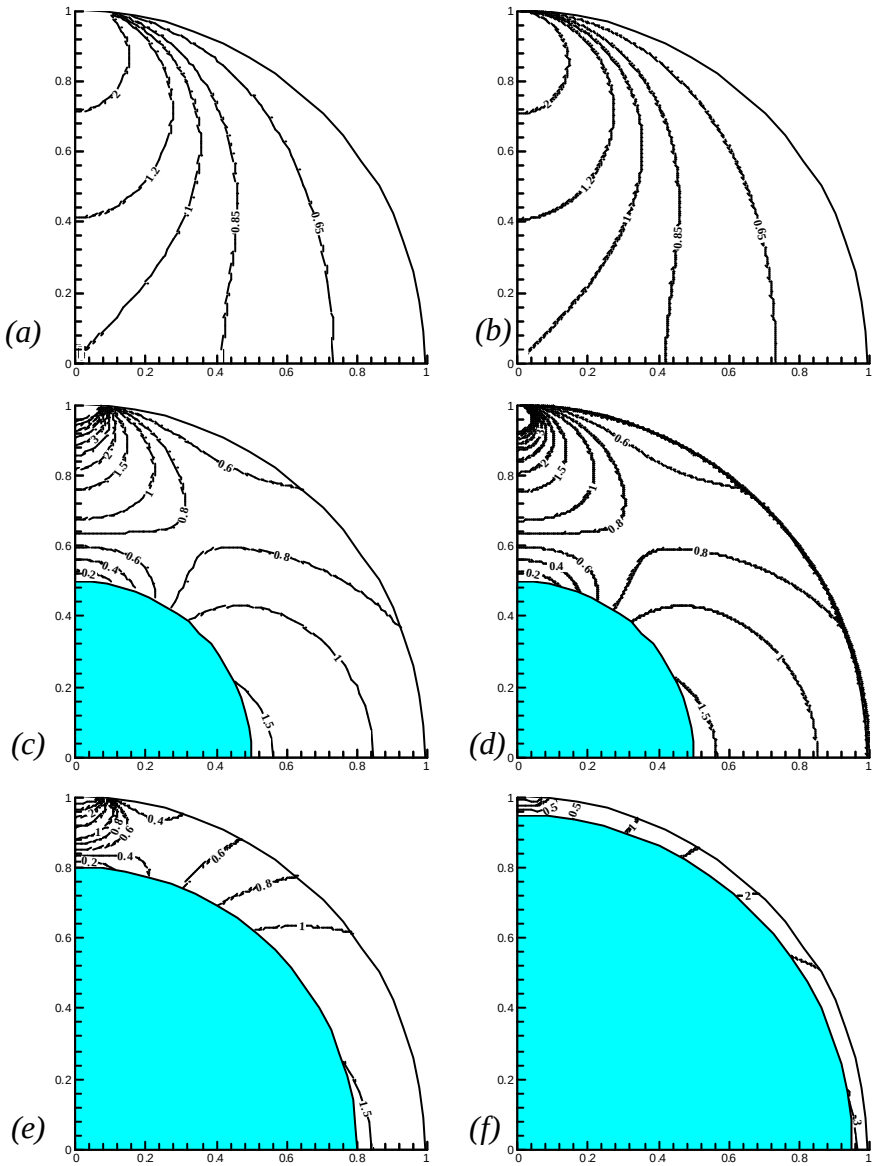

Figure 3.1.5 Contour plots for the normalized rectilinear weight function (1-*e*)*WpR*/2*B*/(1A) (the shaded region represents the gas core): (a) for the single-phase flow; (b) for the single-phase flow(analytical result for point electrodes); (c) for R_i/R = 0.5; (d) for R_i/R = 0.5(analytical series solution calculated up to 200th term for point electrodes); (e) for R_i/R =0.8; (f) R_i/R =0.95.

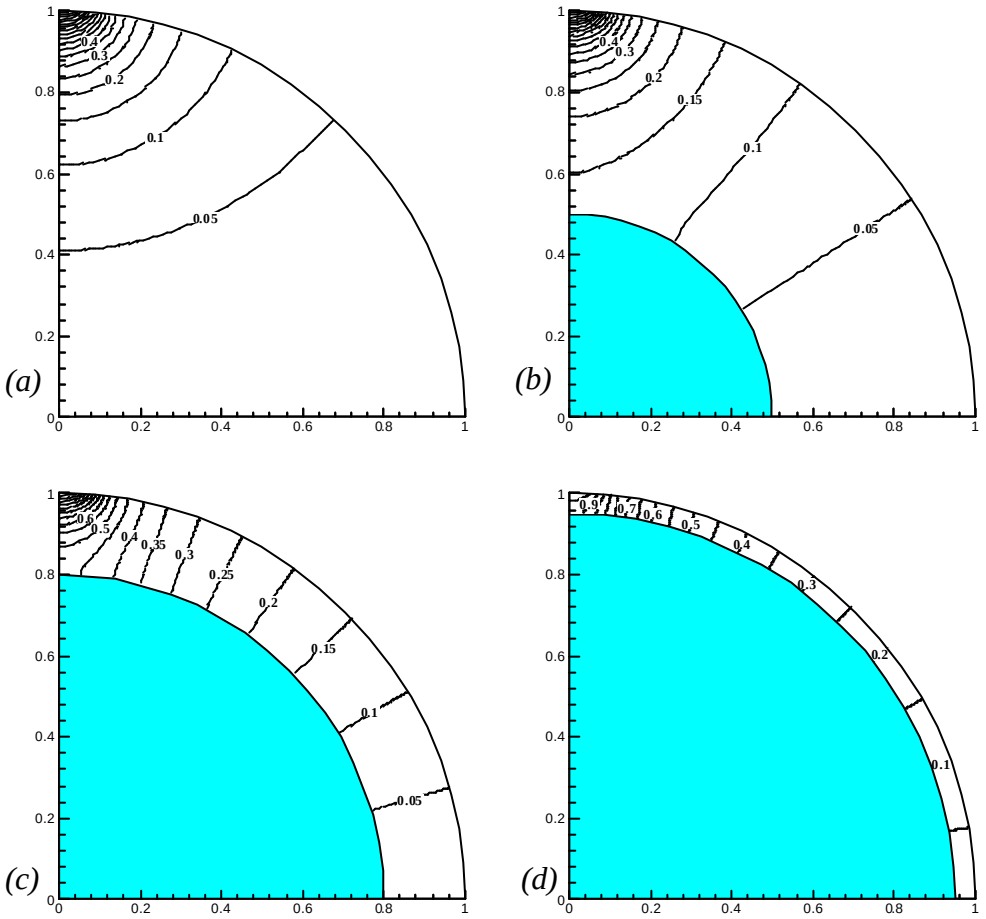

Figure 3.1.6 Contour plots for the normalized virtual potential distribution on the z=0 plane(the shaded region represents the gas core): (a) for the single-phase flow; (b) for R_i/R = 0.5; (c) for R_i/R =0.8; (d) R_i/R =0.95. Contours are advanced by 0.05.

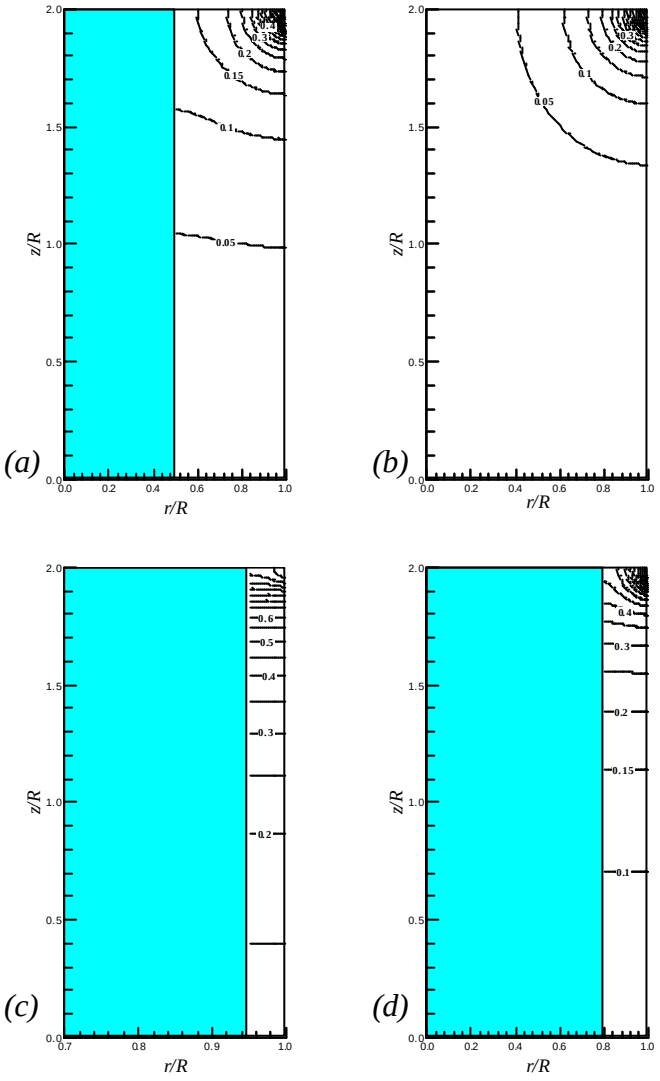

Figure 3.1.7 Contour plots for the normalized virtual potential distribution on the $q=p/2$ plane (the shaded region represents the gas core): (a) for the single-phase flow; (b) for $R_i/R = 0.5$; (c) for $R_i/R = 0.8$; (d) $R_i/R = 0.95$. Contours are advanced by 0.05.

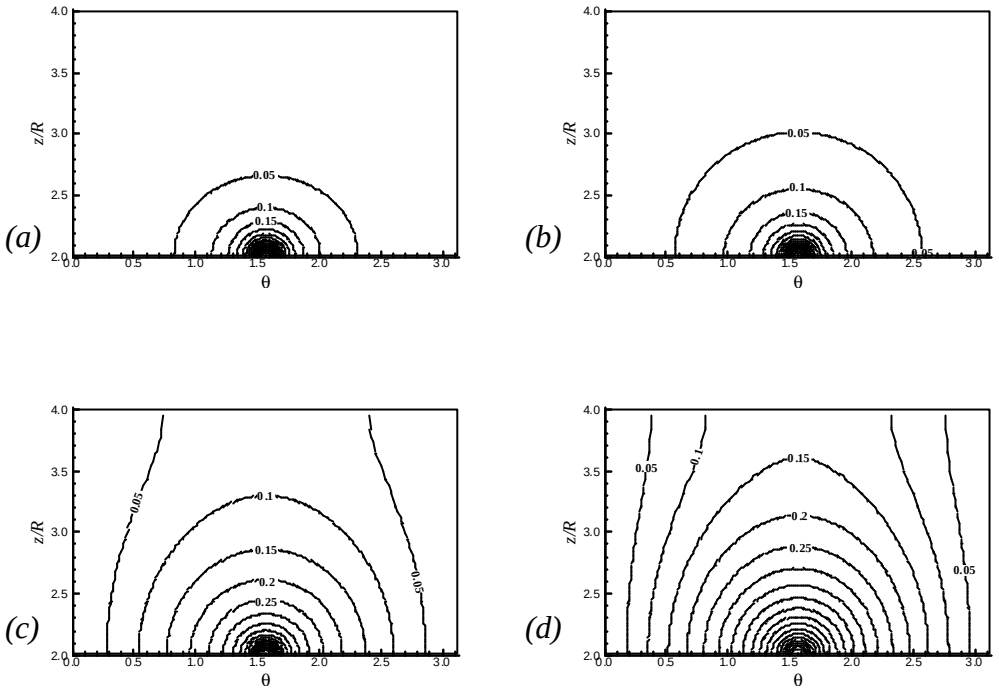

Figure 3.1.8 Contour plots for the normalized virtual potential distribution on the $r=R$ plane: (a) for the single-phase; (b) for R_i/R = 0.5; (c) for R_i/R =0.8; (d) R_i/R =0.95. Contours are advanced by 0.05.

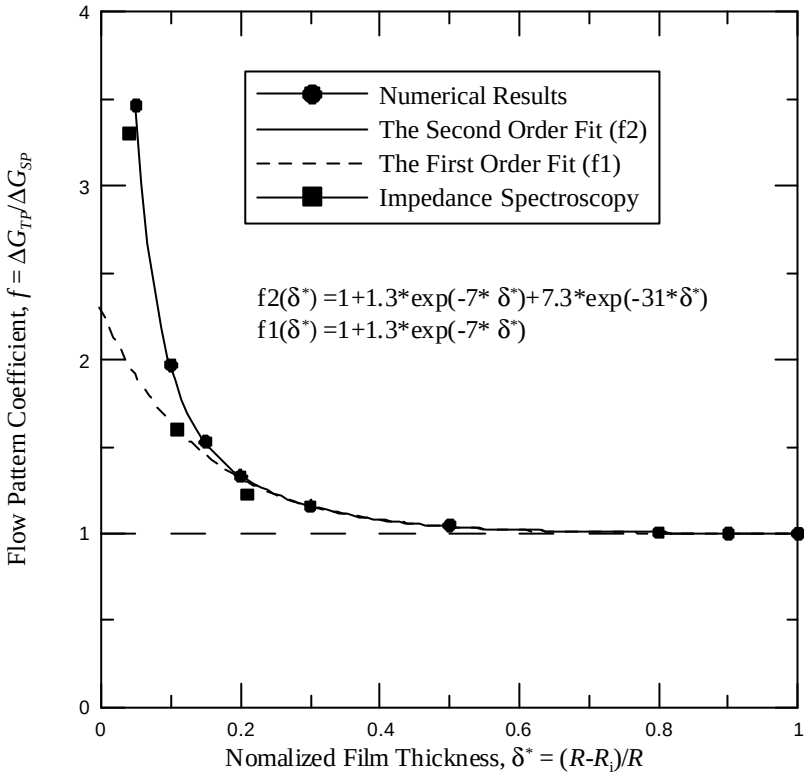

Figure 3.1.9 Plot of the flow pattern coefficient f: symbols, numerical and impedance spectroscopy results; lines, curve fits with exponential functions.

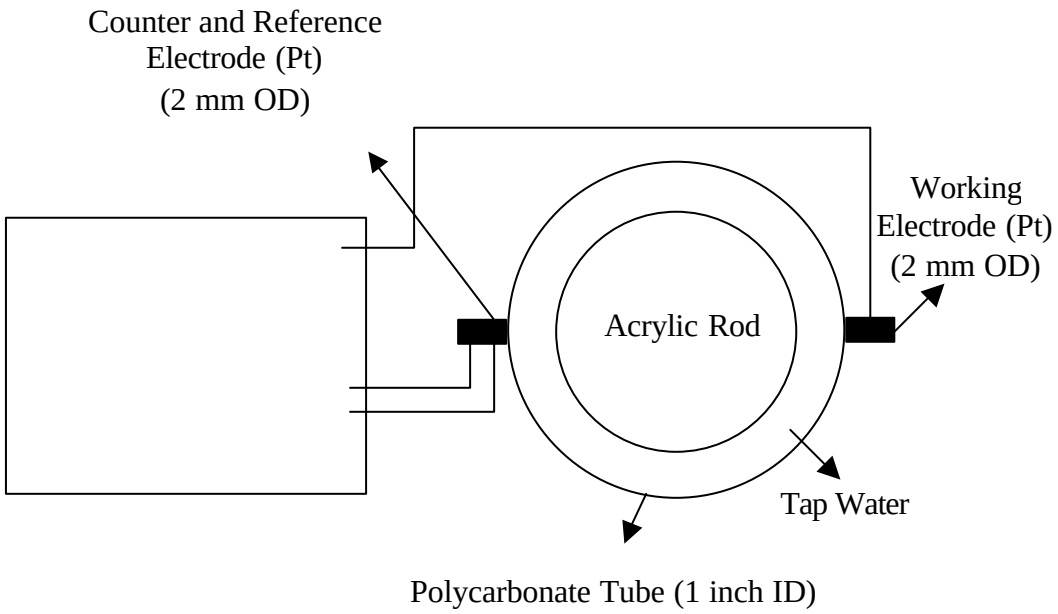

Figure 3.1.10 Schematic diagram for impedance spectroscopy of tap water.

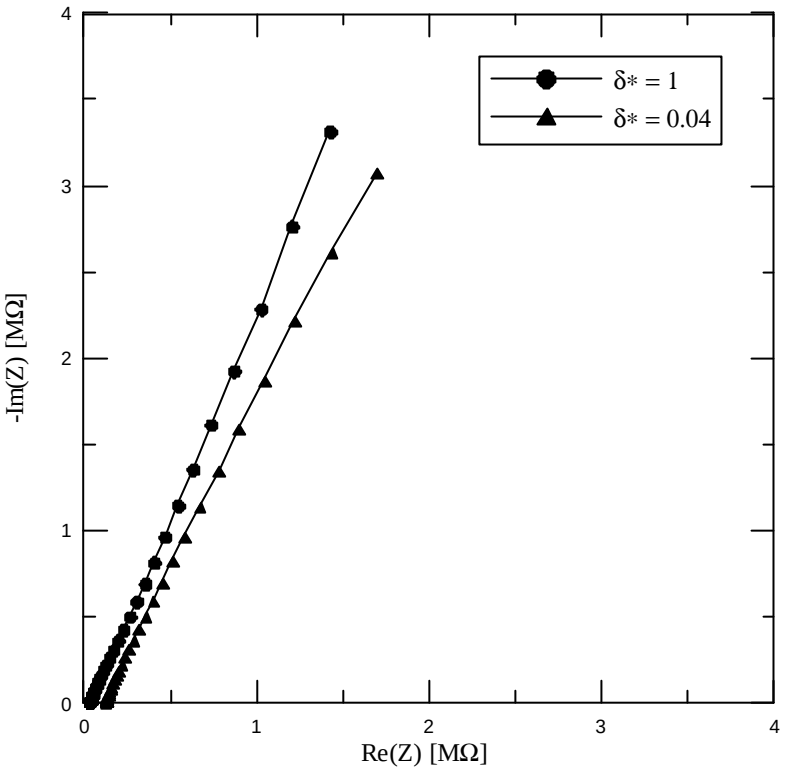

Figure 3.1.11 Nyquist plot from impedance spectroscopy of tap water (23.4°C).

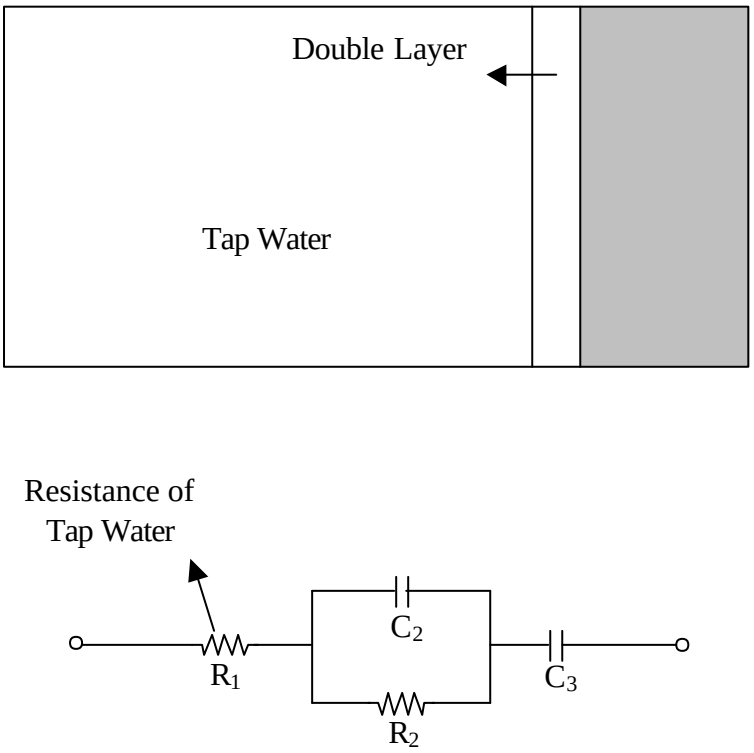

Figure 3.1.12 Circuit modeling of platinum electrodes and tap water system.

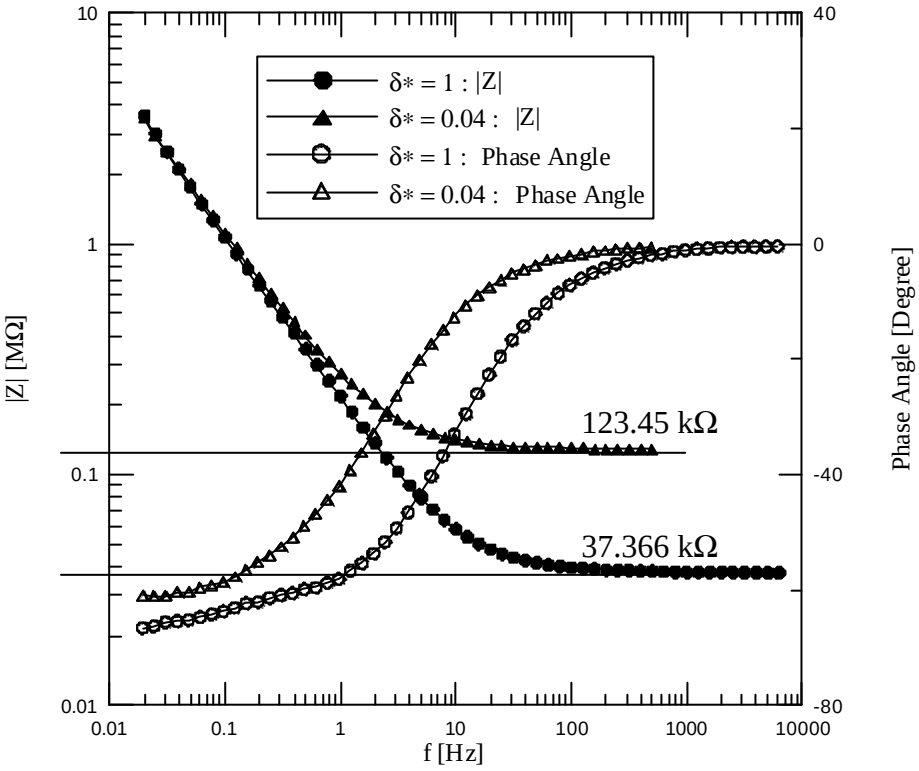

Figure 3.1.13 Bode plot from impedance spectroscopy of tap water (23.4°C).

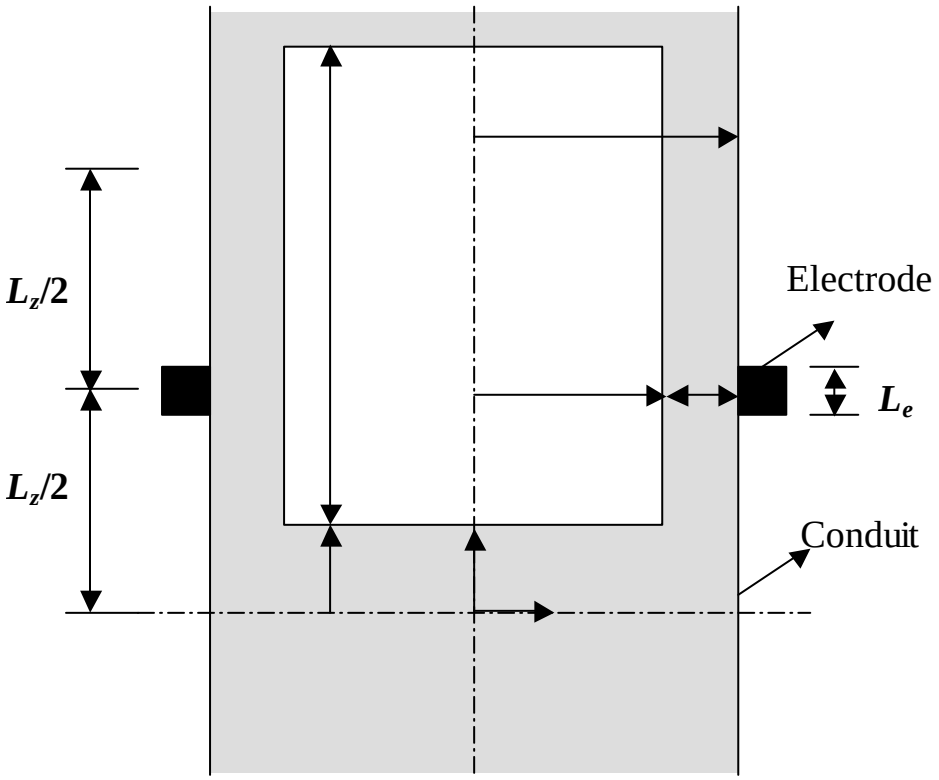

Figure 3.2.1 Schematics for the computational domain.

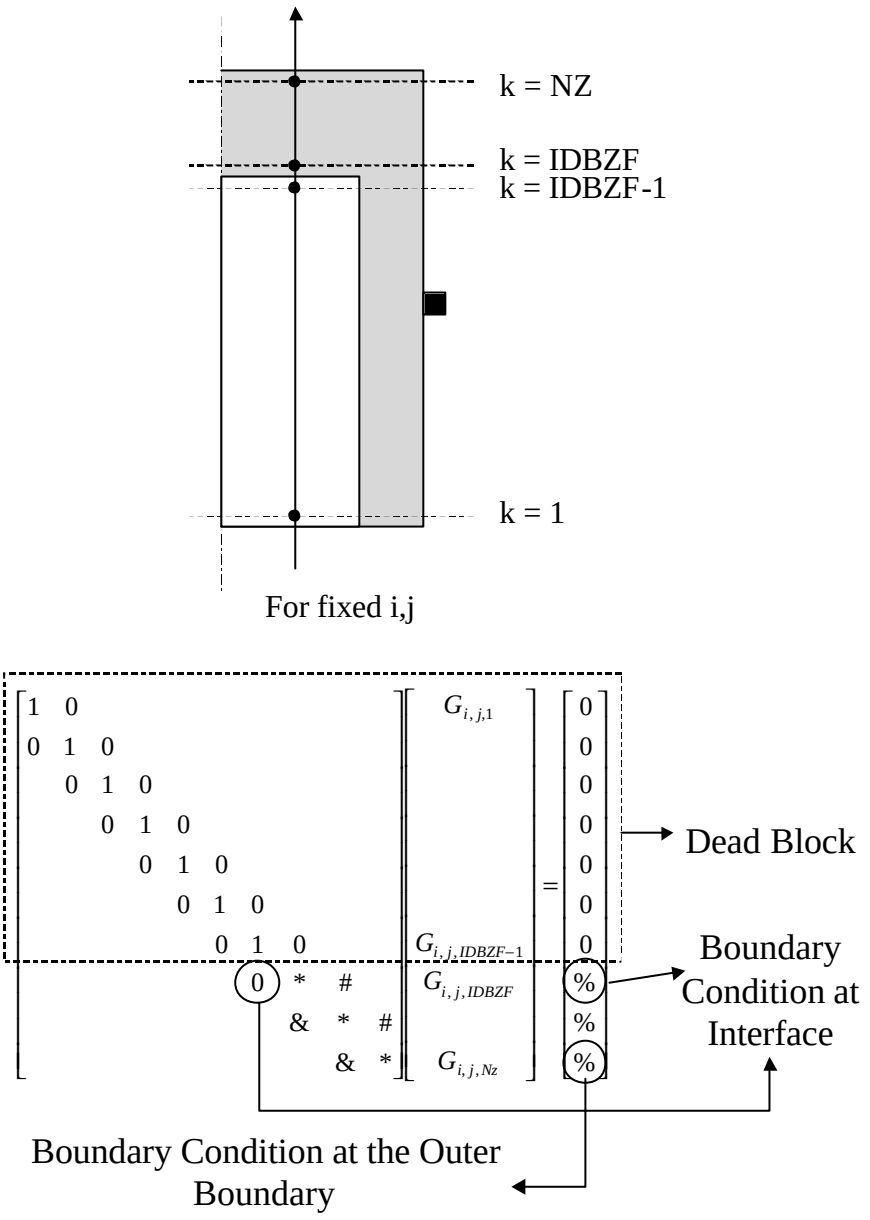

Figure 3.2.2 Dead block treatment.

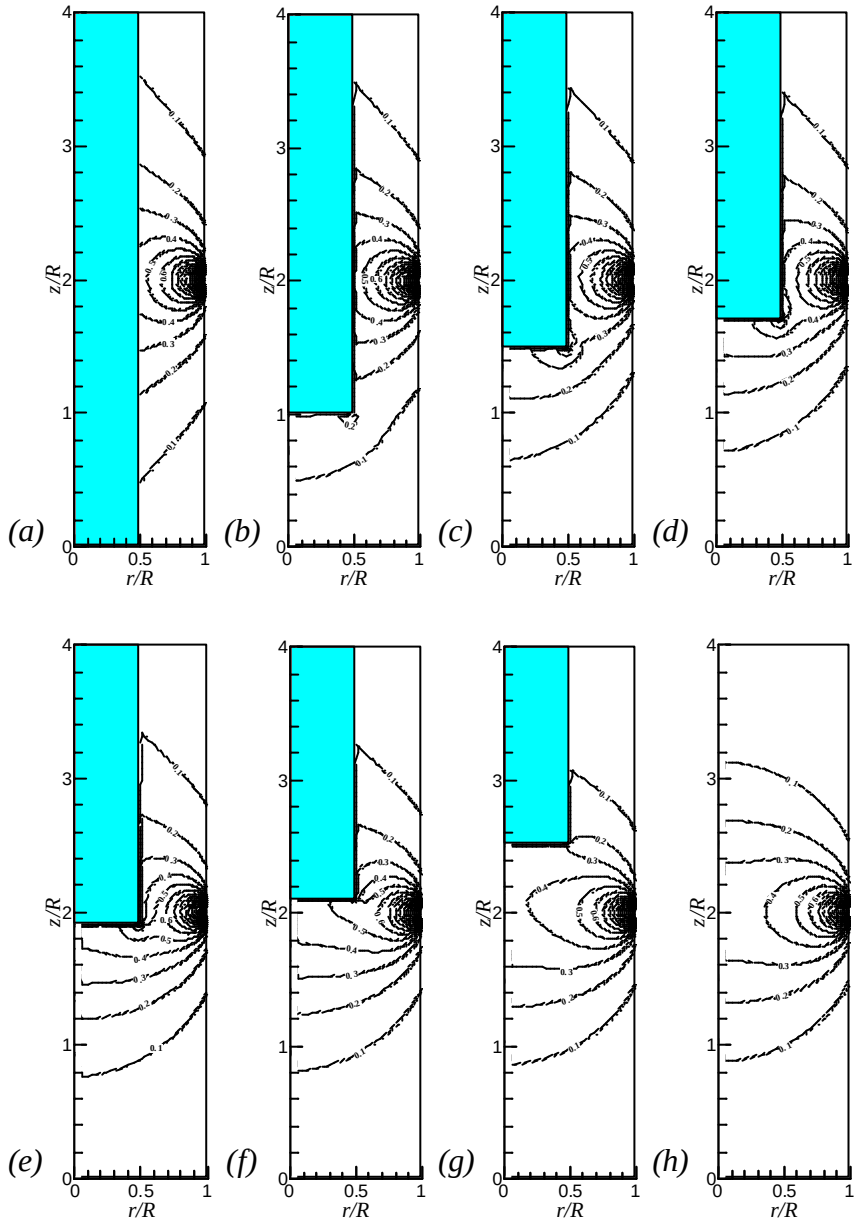

Figure 3.2.3 Contour plots of the axial weight function for the non-dimensional film thickness d^*=0.5 (the shaded region represents a rising bubble): (a) for L^*=0; (b) for L^*=1.0; (c) for L^*=1.5; (d) for L^*=1.7; (e) for L^*=1.9; (f) for L^*=2.1; (g) for L^*=2.5; (h) for L^*=4. Contours are advanced by 0.1.

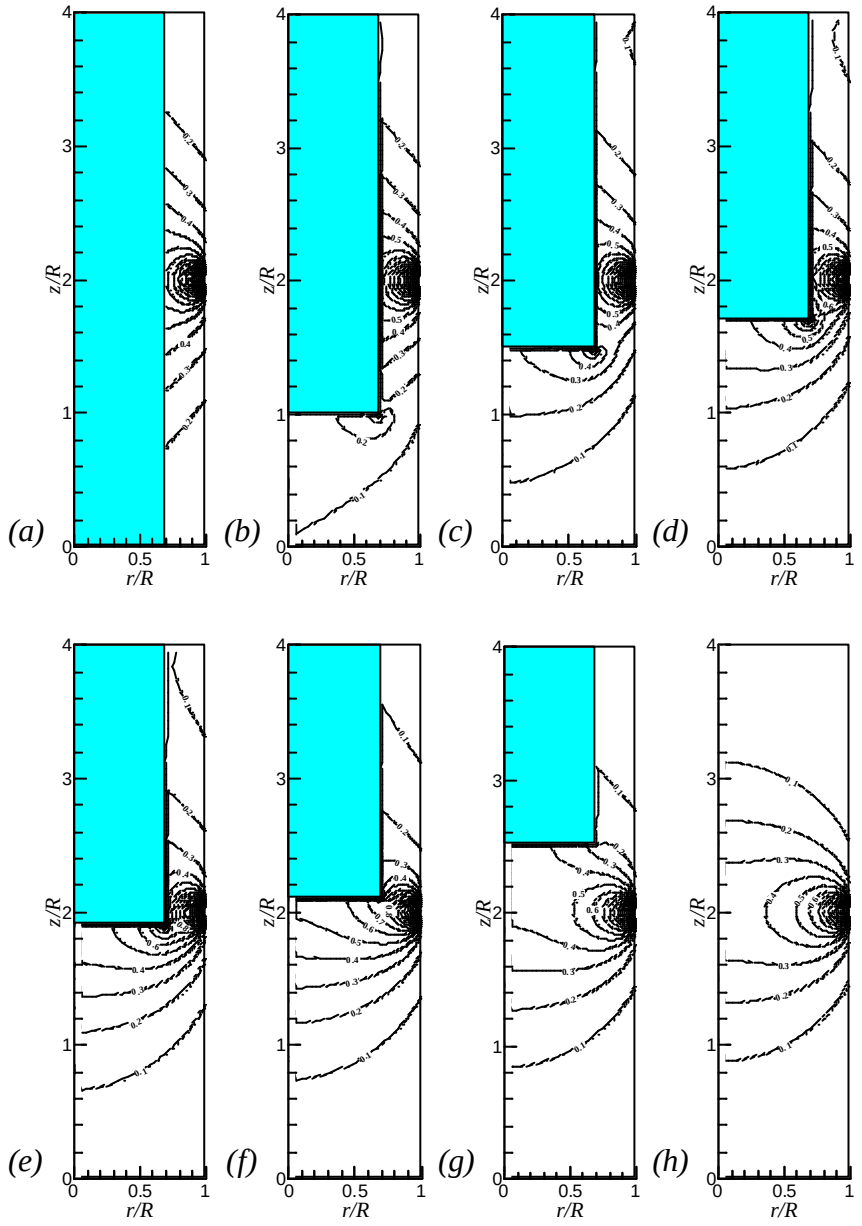

Figure 3.2.4 Contour plots of the axial weight function for the non-dimensional film thickness d^*=0.3 (the shaded region represents a rising bubble): (a) for L^*=0; (b) for L^*=1.0; (c) for L^*=1.5; (d) for L^*=1.7; (e) for L^*=1.9; (f) for L^*=2.1; (g) for L^*=2.5; (h) for L^*=4. Contours are advanced by 0.1.

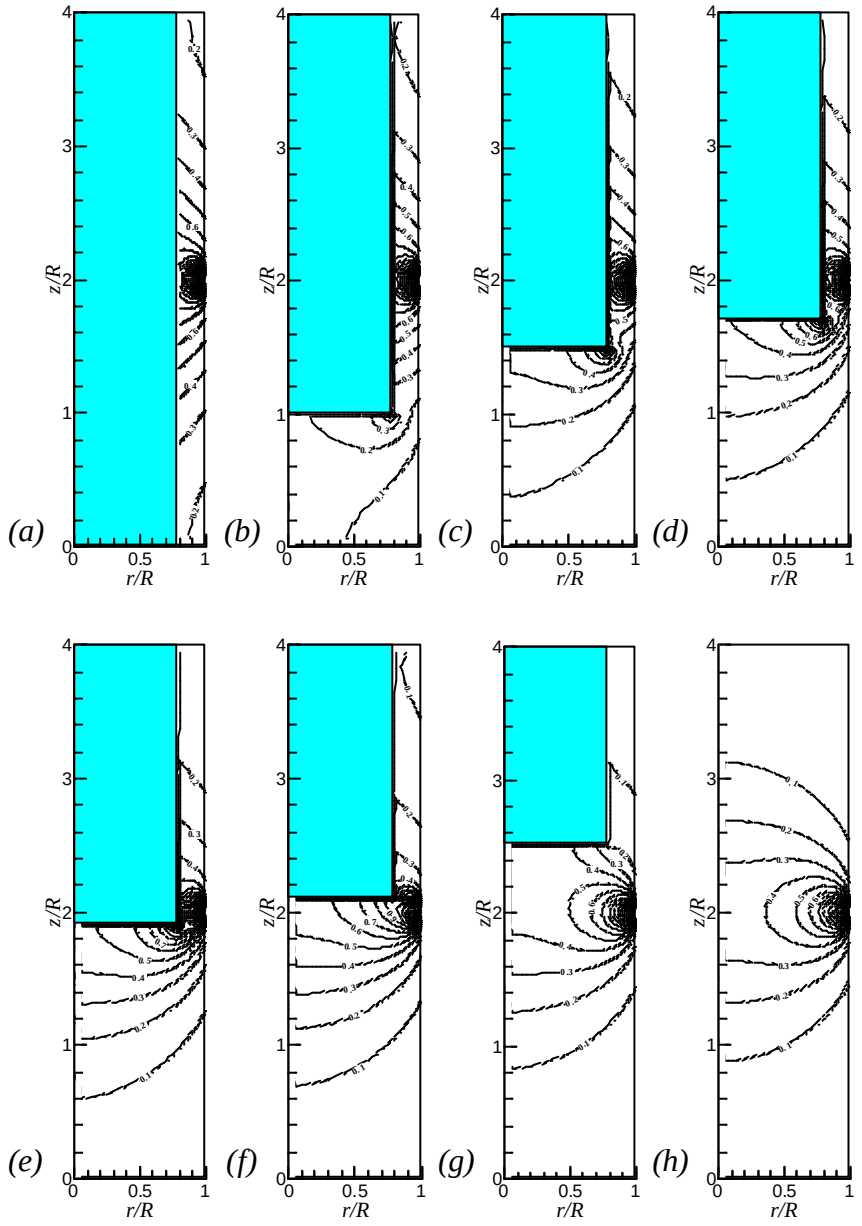

Figure 3.2.5 Contour plots of the axial weight function for the non-dimensional film thickness d^*=0.2 (the shaded region represents a rising bubble): (a) for L^*=0; (b) for L^*=1.0; (c) for L^*=1.5; (d) for L^*=1.7; (e) for L^*=1.9; (f) for L^*=2.1; (g) for L^*=2.5; (h) for L^*=4. Contours are advanced by 0.1.

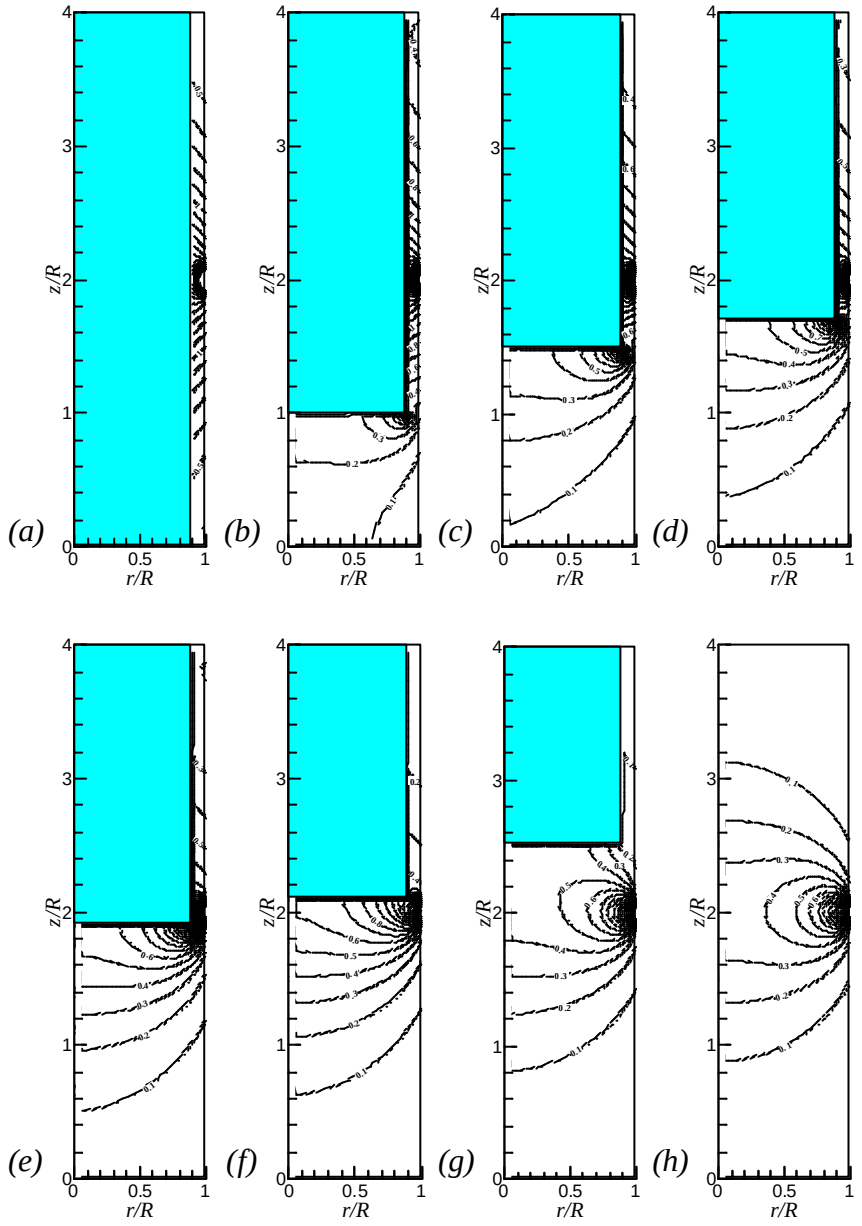

Figure 3.2.6 Contour plots of the axial weight function for the non-dimensional film thickness d^*=0.1 (the shaded region represents a rising bubble): (a) for L^*=0; (b) for L^*=1.0; (c) for L^*=1.5; (d) for L^*=1.7; (e) for L^*=1.9; (f) for L^*=2.1; (g) for L^*=2.5; (h) for L^*=4. Contours are advanced by 0.1.

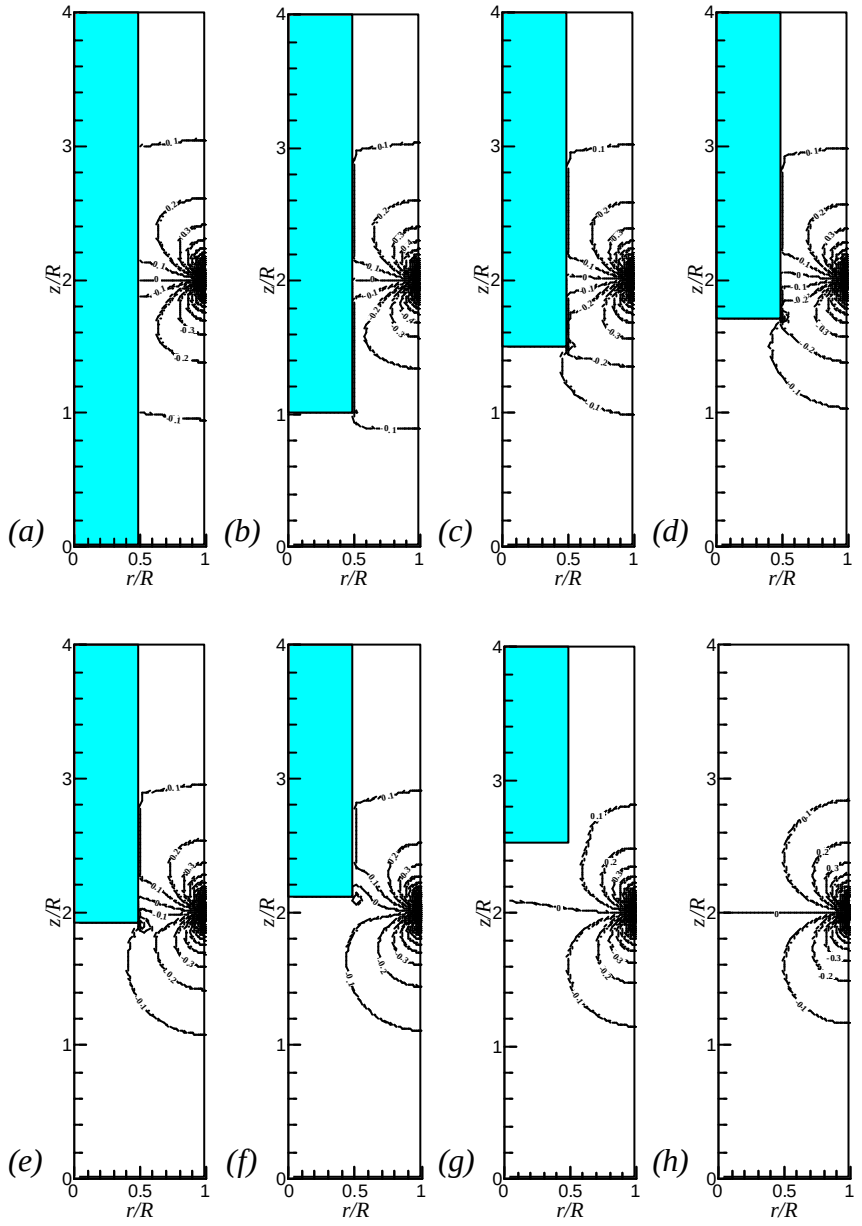

Figure 3.2.7 Contour plots of the radial weight function for the non-dimensional film thickness d^*=0.5 (the shaded region represents a rising bubble): (a) for L^*=0; (b) for L^*=1.0; (c) for L^*=1.5; (d) for L^*=1.7; (e) for L^*=1.9; (f) for L^*=2.1; (g) for L^*=2.5; (h) for L^*=4. Contours are advanced by 0.1.

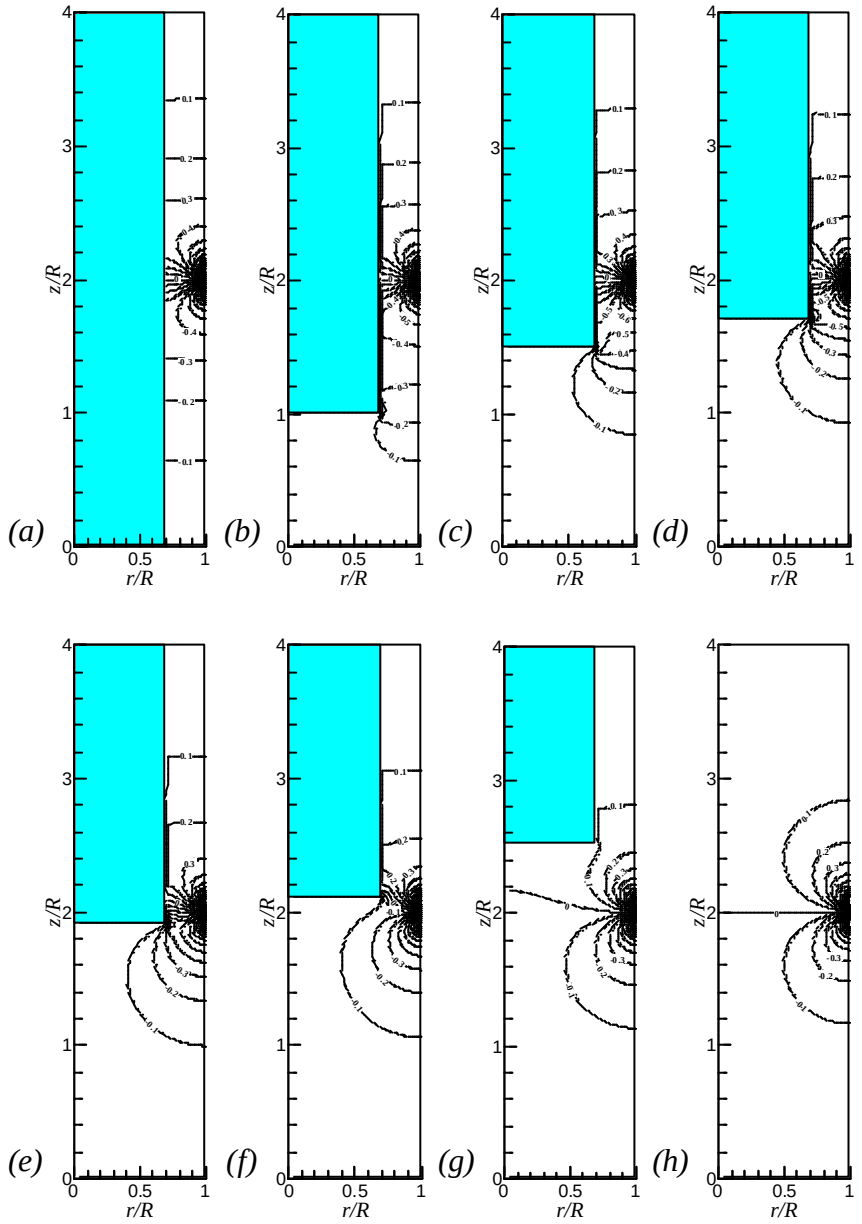

Figure 3.2.8 Contour plots of the radial weight function for the non-dimensional film thickness d^*=0.3 (the shaded region represents a rising bubble): (a) for L^*=0; (b) for L^*=1.0; (c) for L^*=1.5; (d) for L^*=1.7; (e) for L^*=1.9; (f) for L^*=2.1; (g) for L^*=2.5; (h) for L^*=4. Contours are advanced by 0.1.

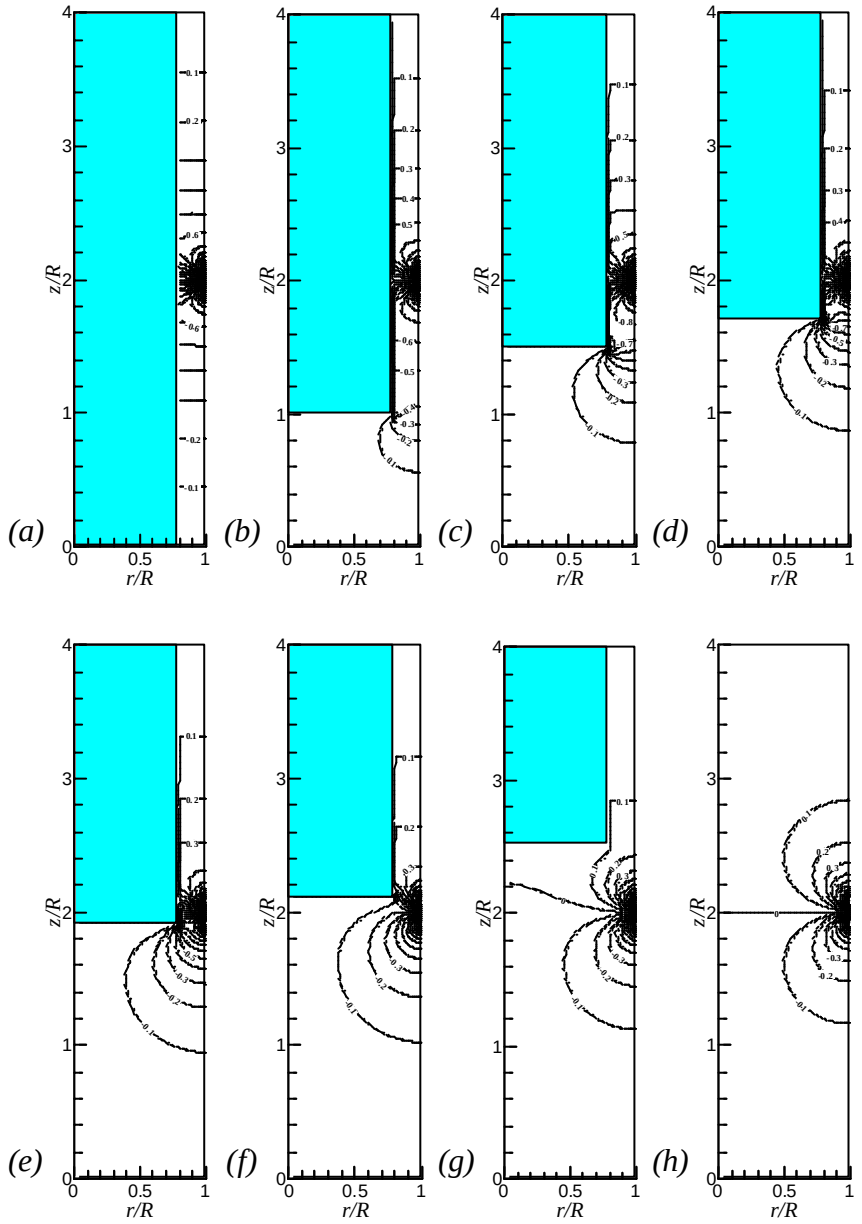

Figure 3.2.9 Contour plots of the radial weight function for the non-dimensional film thickness d^*=0.2 (the shaded region represents a rising bubble): (a) for L^*=0; (b) for L^*=1.0; (c) for L^*=1.5; (d) for L^*=1.7; (e) for L^*=1.9; (f) for L^*=2.1; (g) for L^*=2.5; (h) for L^*=4. Contours are advanced by 0.1.

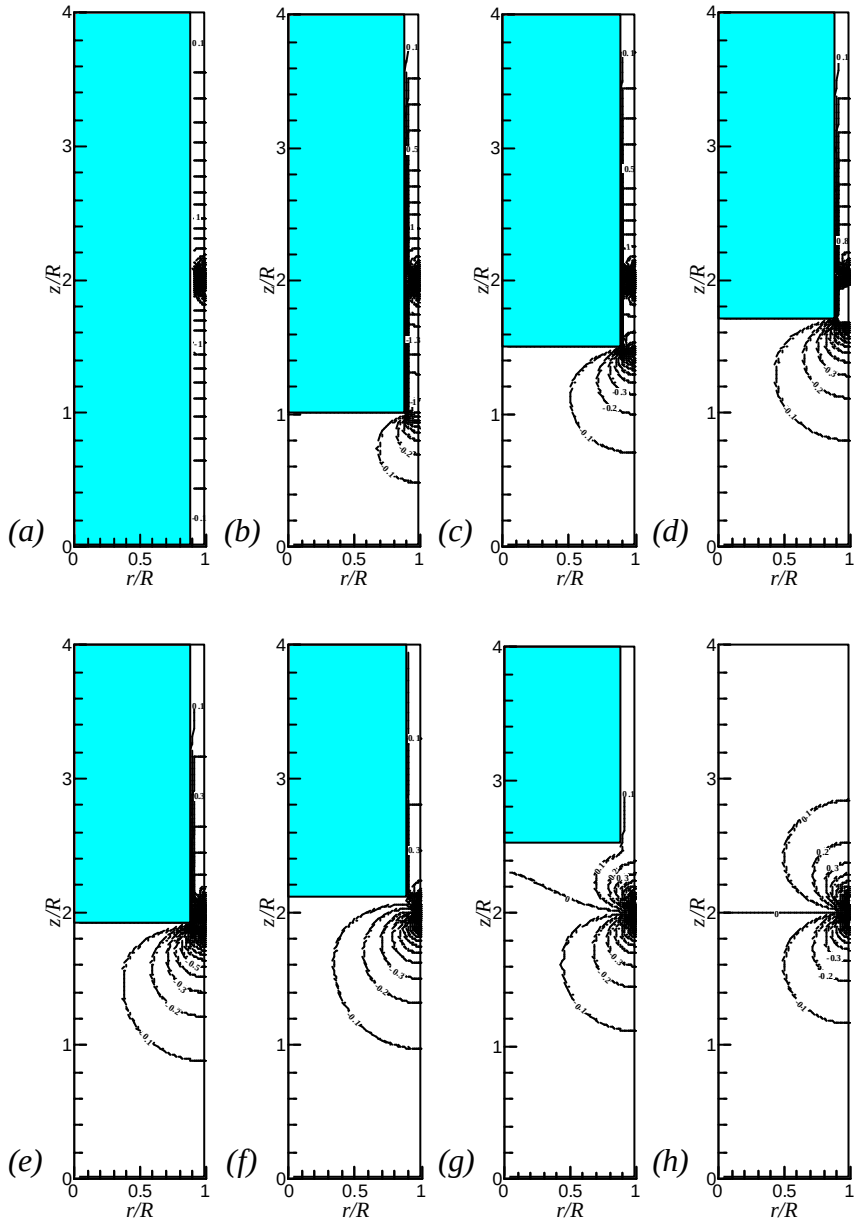

Figure 3.2.10 Contour plots of the radial weight function for the non-dimensional film thickness d^*=0.1 (the shaded region represents a rising bubble): (a) for L^*=0; (b) for L^*=1.0; (c) for L^*=1.5; (d) for L^*=1.7; (e) for L^*=1.9; (f) for L^*=2.1; (g) for L^*=2.5; (h) for L^*=4. Contours are advanced by 0.1.

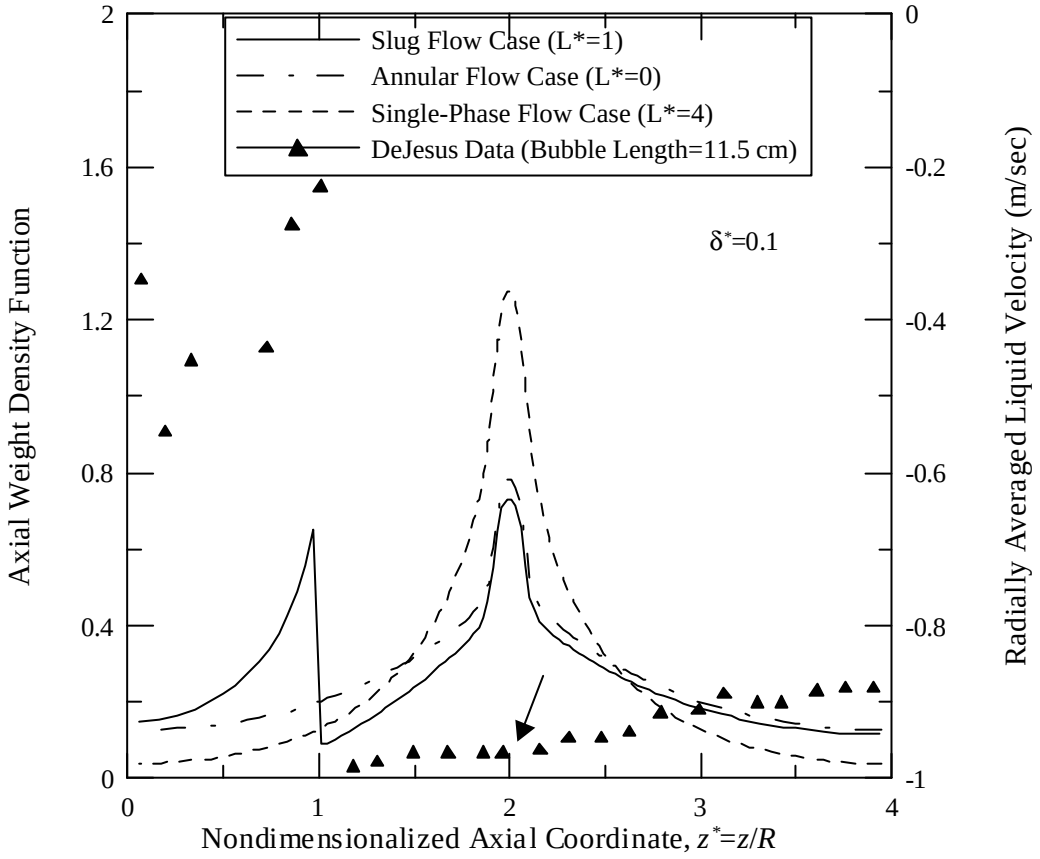

Figure 3.2.11 The axial weight density function for d^*=0.1 and L^*=1.0.

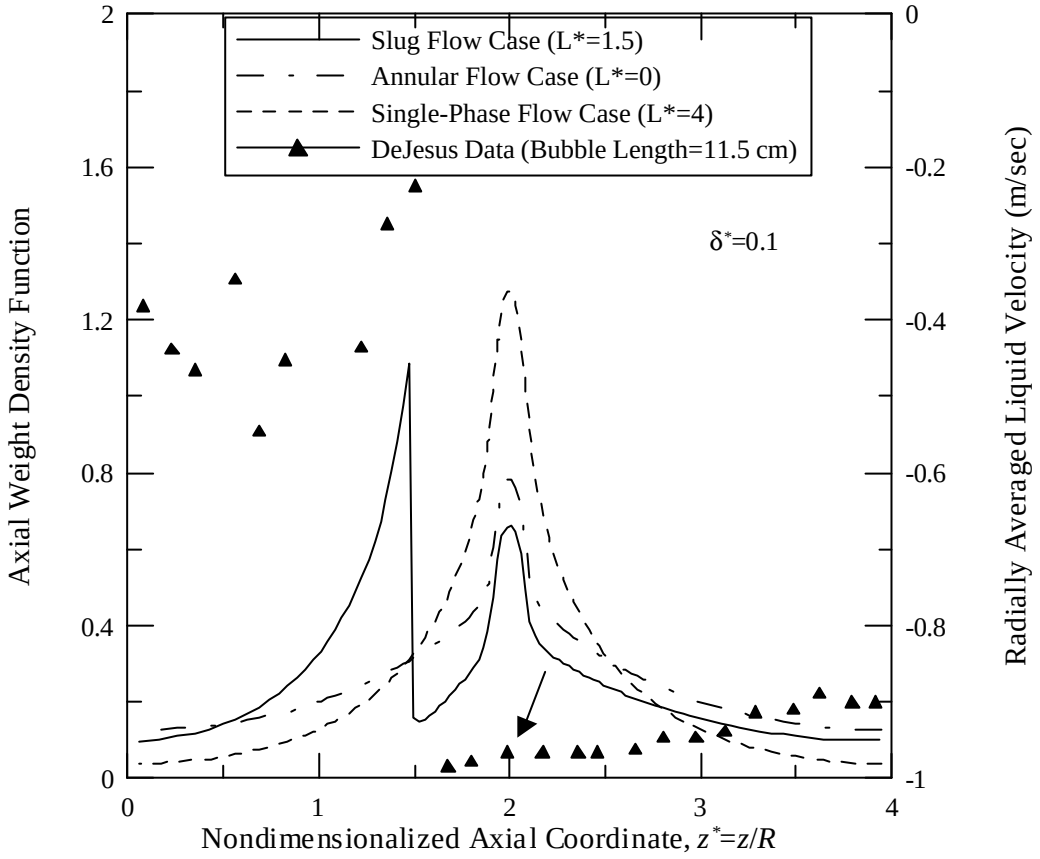

Figure 3.2.12 The axial weight density function for d^*=0.1 and L^*=1.5.

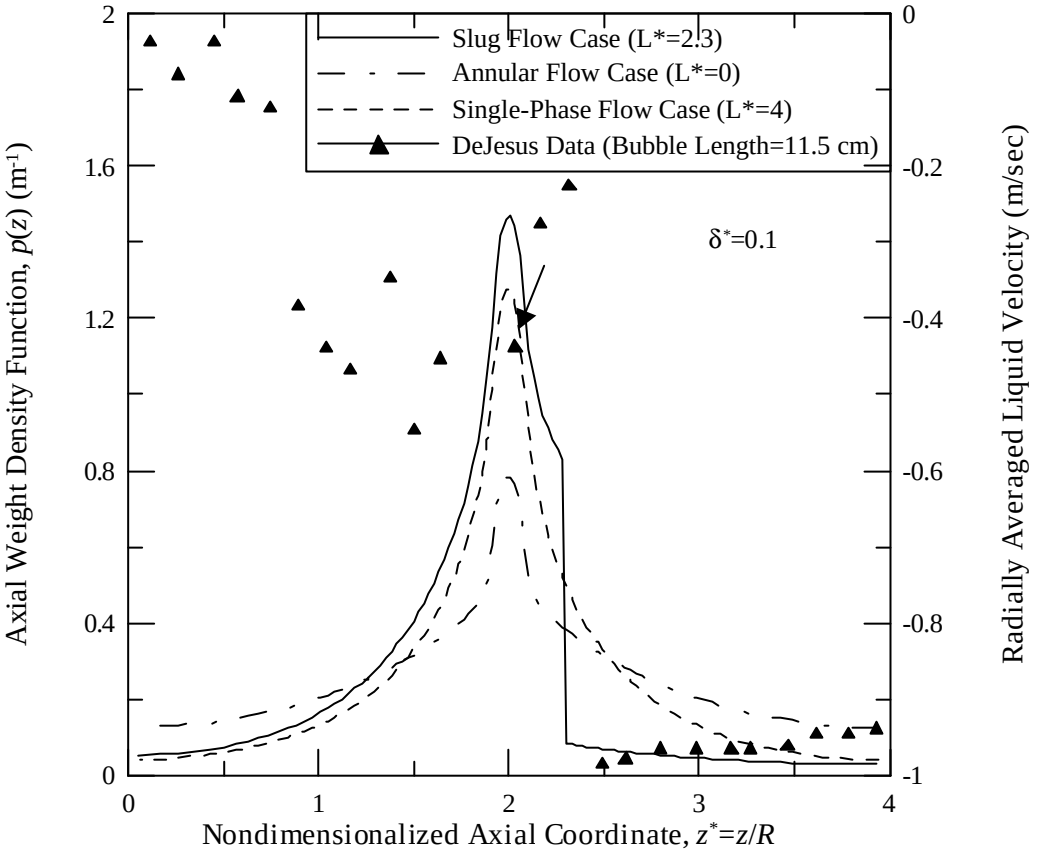

Figure 3.2.13 The axial weight density function for d^*=0.1 and L^*=2.3.

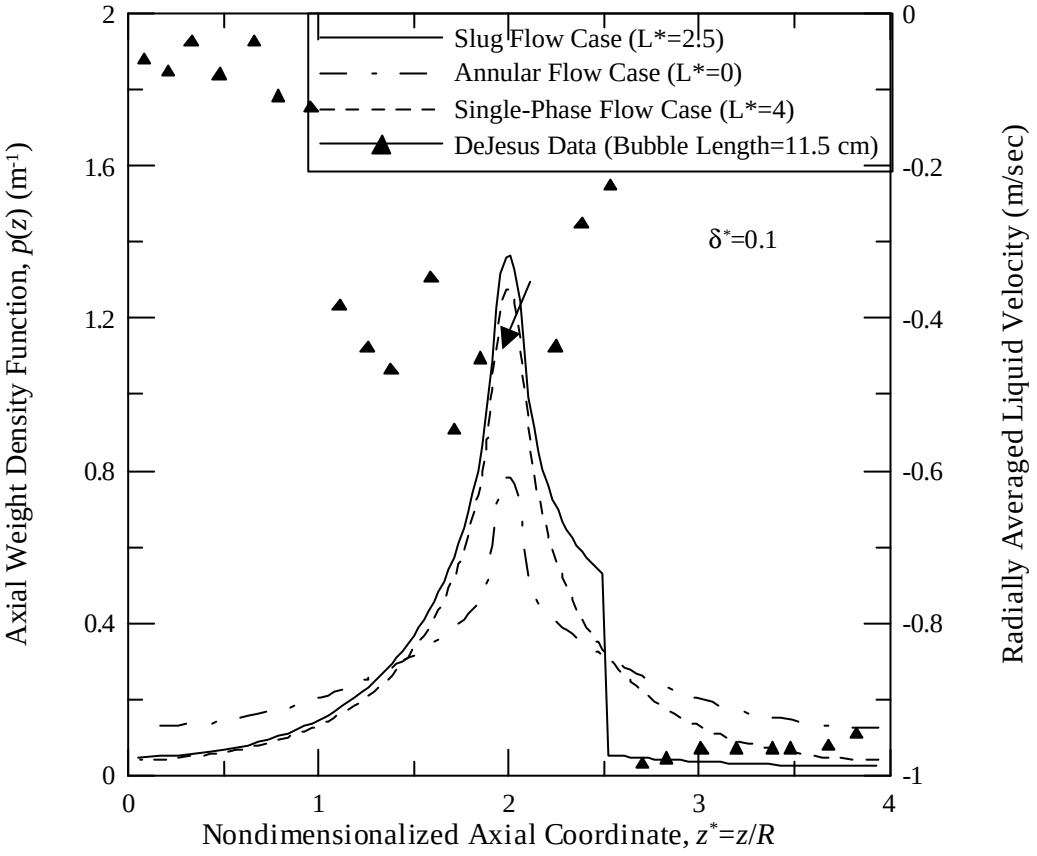

Figure 3.2.14 The axial weight density function for d^*=0.1 and L^*=2.5.

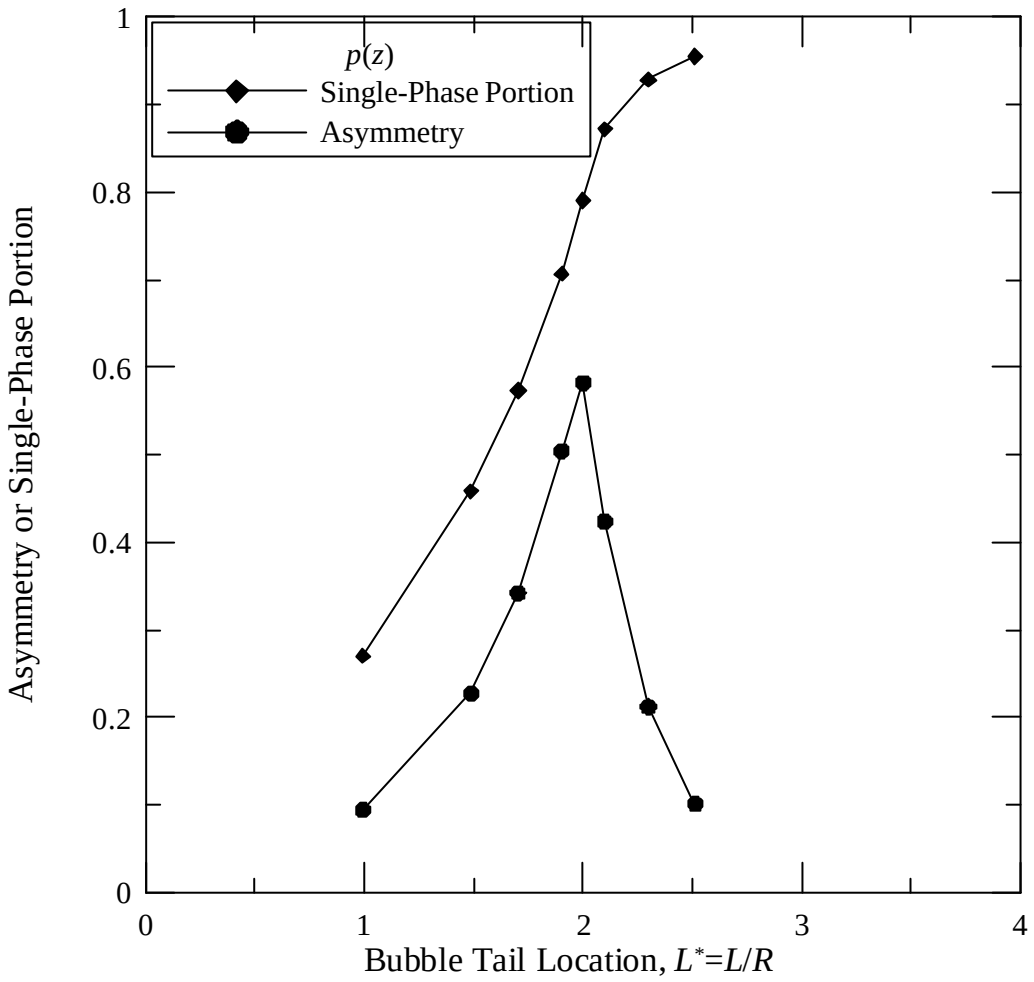

Figure 3.2.15 Asymmetry and single-phase portion of the axial weight density function for d^*=0.1.

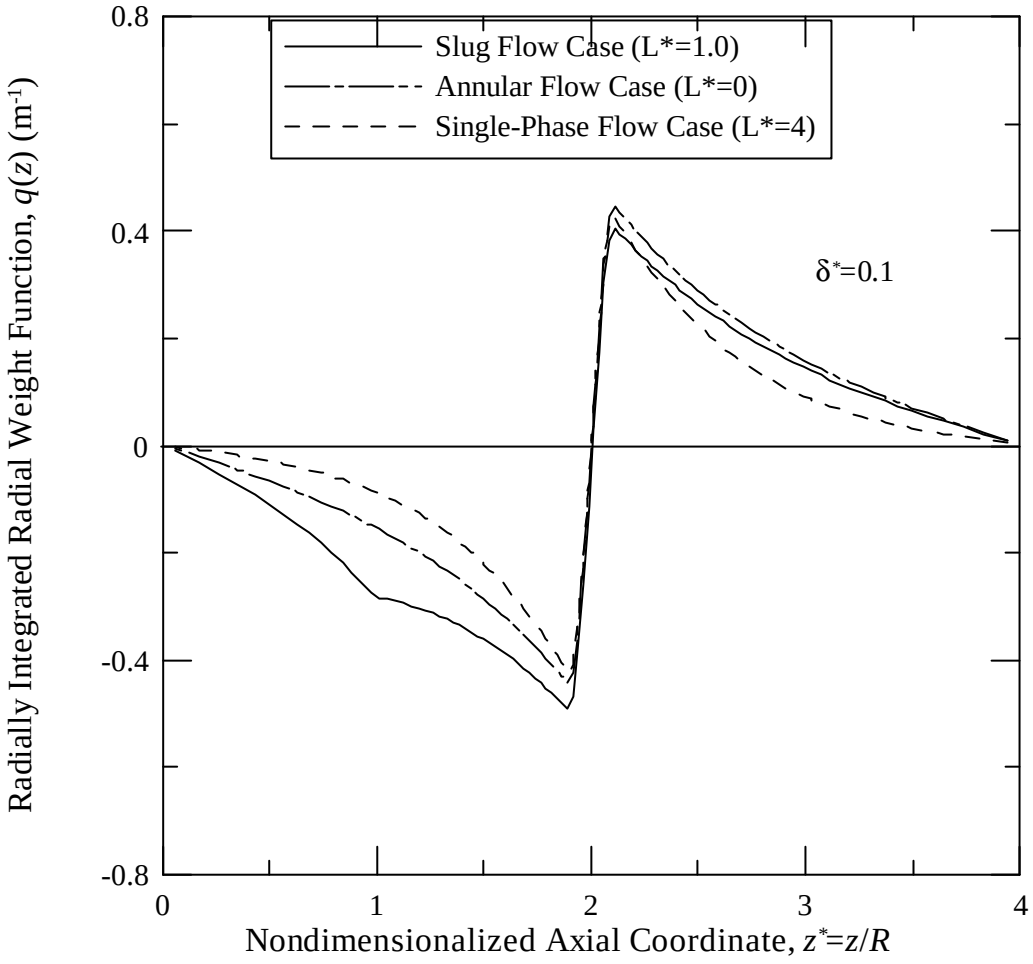

Figure 3.2.16 Radially integrated radial weight function for d^*=0.1 and L^*=1.0.

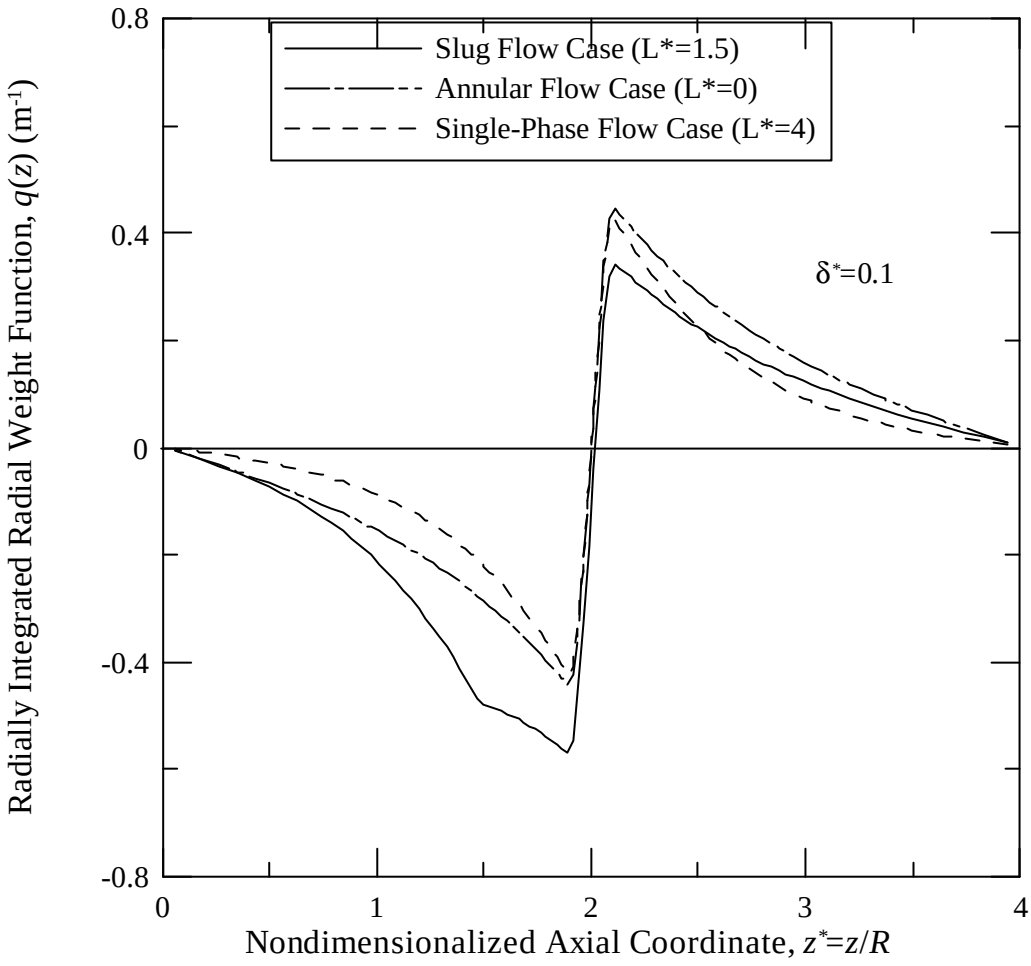

Figure 3.2.17 Radially integrated radial weight function for d^*=0.1 and L^*=1.5.

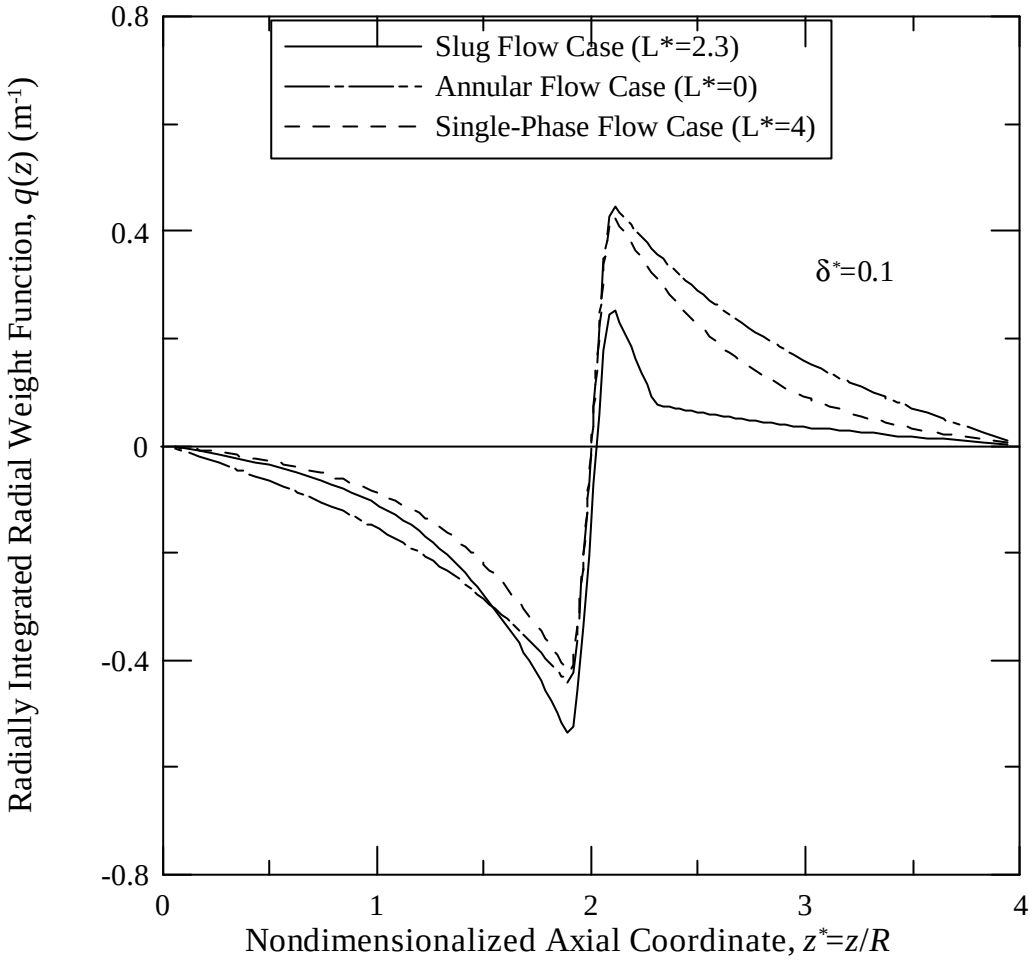

Figure 3.2.18 Radially integrated radial weight function for d^*=0.1 and L^*=2.3.

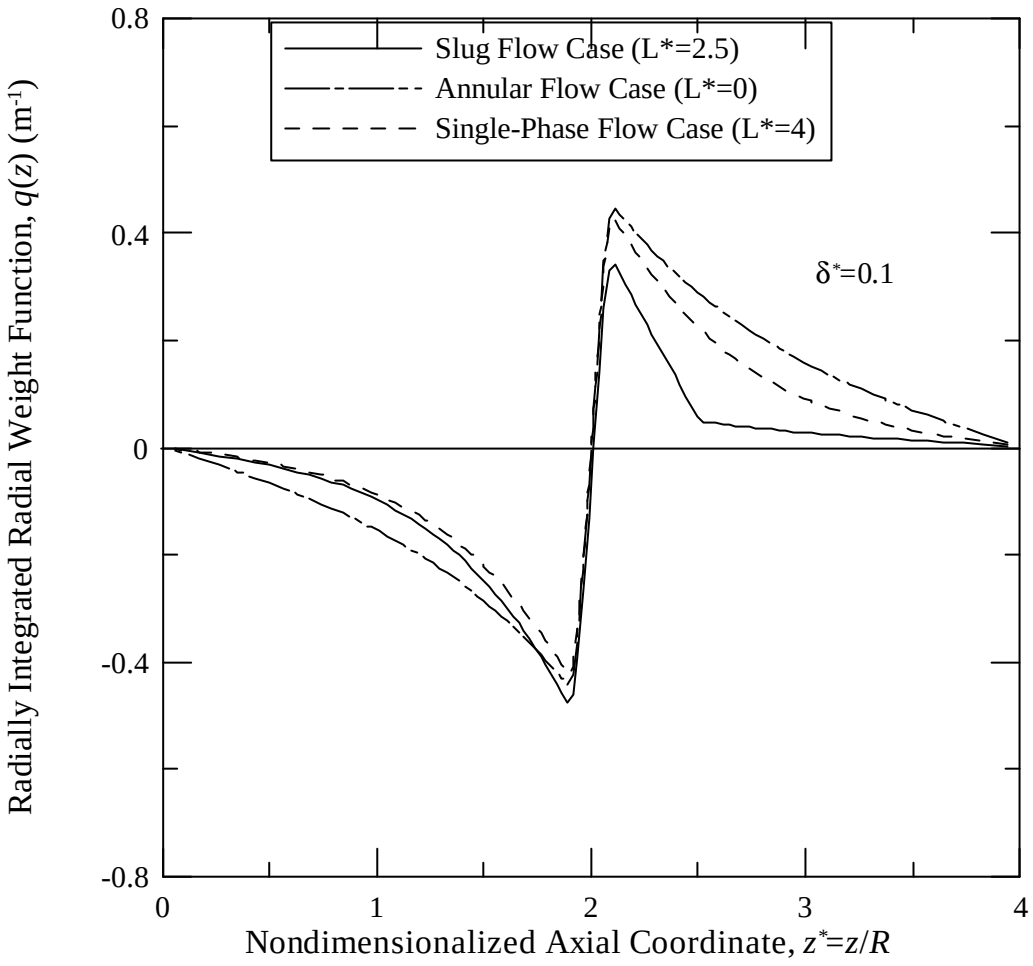

Figure 3.2.19 Radially integrated radial weight function for d^*=0.1 and L^*=2.5.

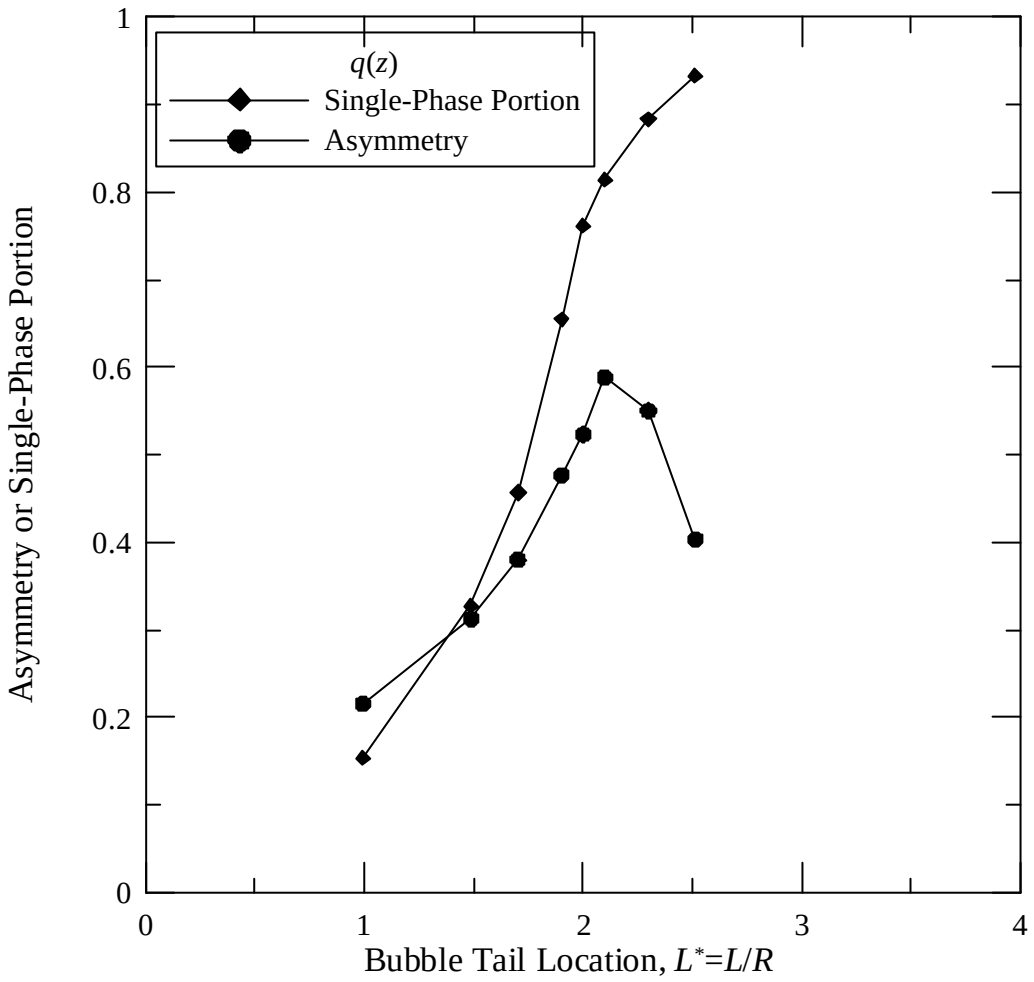

Figure 3.2.20 Asymmetry and single-phase portion of the radially averaged radial weight function for d^*=0.1.

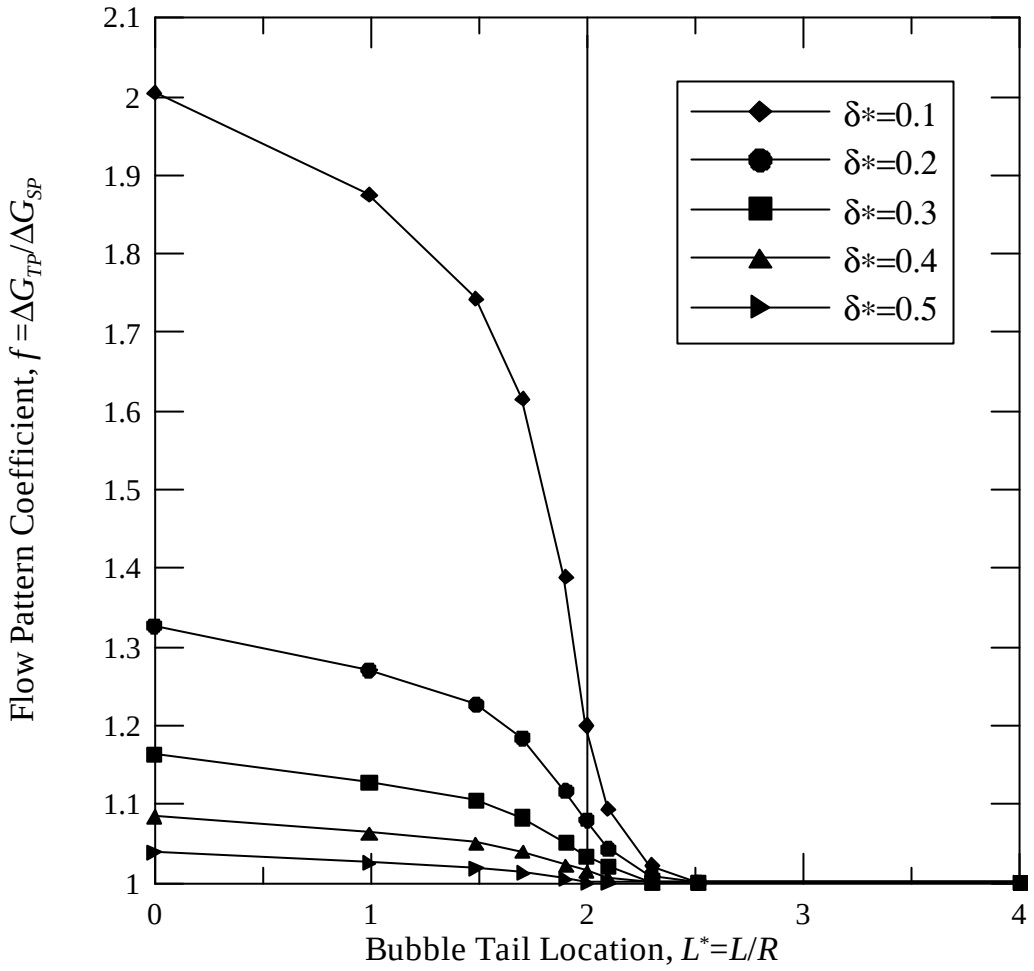

Figure 3.2.21 The flow pattern coefficient as a function of d^* and L^*.

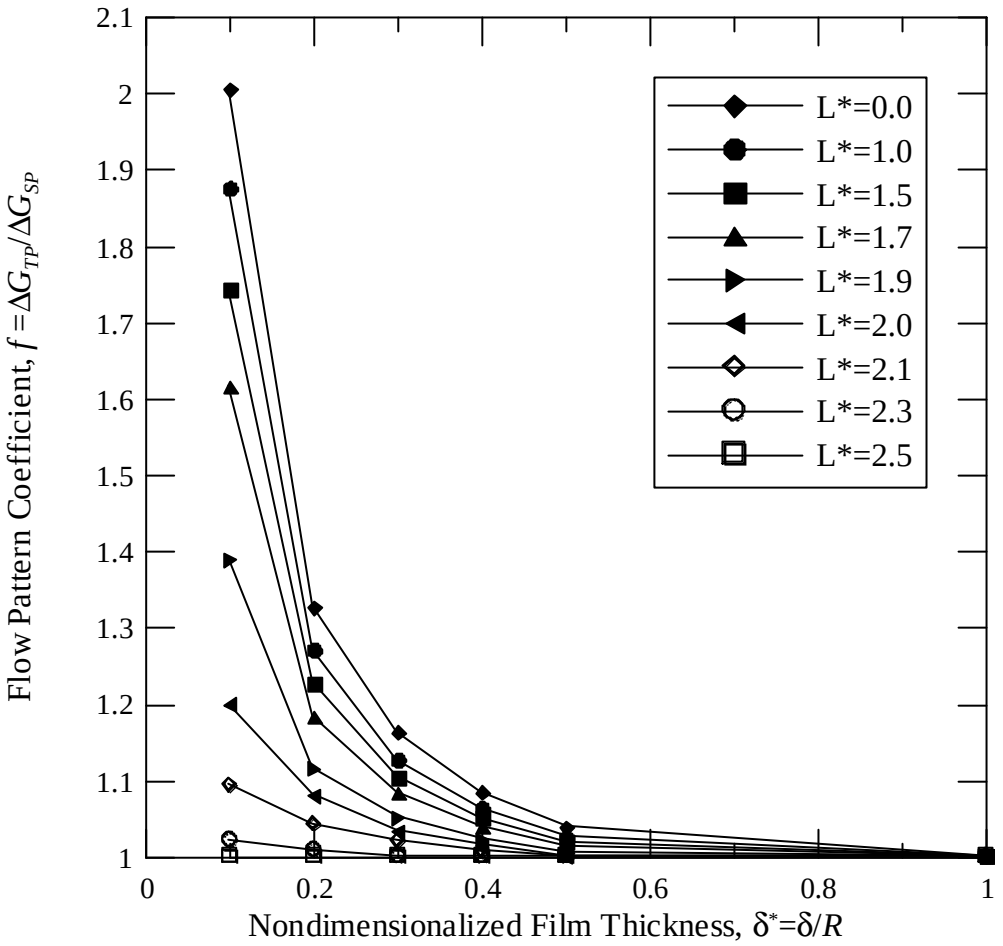

Figure 3.2.22 The flow pattern coefficient as a function of d^* and L^*.

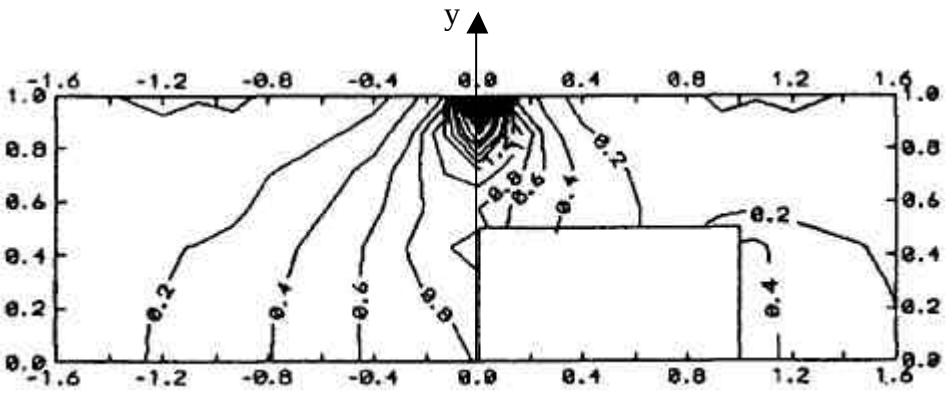

Figure 3.2.23 Distribution of the virtual current $\frac{\partial G}{\partial y}$ for a square bubble with length 0.5 when the nose reaches the electrode plane (**Zhang** 1998).